Nb–C thin films prepared by DC-MS and HiPIMS: synthesis, structure, and tribomechanical properties

N. Sala[1*], M.D. Abad[1], J.C. Sánchez-López[2], J. Caro[3], C. Colominas[1,4]

[1]*Grup d'Enginyeria de Materials (GEMAT), Institut Químic de Sarrià, Universitat Ramon Llull, Via Augusta 390, Barcelona 08017, Spain (neus.sala@iqs.url.edu, manuel.abad@iqs.url.edu)*

[2]*Instituto de Ciencia de Materiales de Sevilla, CSIC-Universidad de Sevilla, Avda. Américo Vespucio 49, 41092 Sevilla, Spain (jcslopez@icmse.csic.es)*

[3]*Eurecat, Centre Tecnològic de Catalunya, Unit of Metallic and Ceramic Materials, Plaça de la Ciència 2, 08243 Manresa, Spain. (jaume.caro@eurecat.org)*

[4]*Flubetech S.L. Carrer Montsià 23, 08211 Castellar del Vallès, Barcelona, Spain (carles.colominas@iqs.url.edu)*

**Corresponding author:* neus.sala@iqs.url.edu

Abstract

Nanostructured Nb–C thin films were prepared by direct current magnetron sputtering (DC-MS) and high-power impulse magnetron sputtering (HiPIMS). The films were characterized in depth by X-ray diffraction (XRD), grazing incidence X-ray diffraction, scanning electron microscopy, atomic force microscopy, electron probe microanalysis, and Raman spectroscopy. The mechanical properties were measured by nanoindentation, and the tribological properties were measured by pin-on-disk tests in ambient air. The wear tracks and ball scars were analyzed by Raman spectroscopy to elucidate the

tribochemical reactions that occurred at the contact area and to determine the wear mechanism for each specimen type. The thermal stability of the coatings was studied up to 1000 °C using Raman spectroscopy and XRD. The samples prepared by DC-MS were very dense, and the phase composition changed from purely nanocrystalline (Nb_2C and NbC) to a mixture of NbC crystals embedded in an amorphous carbon-based matrix (NbC/a-C(:H)). However, the samples prepared by HiPIMS developed a marked columnar morphology with a NbC/a-C(:H) nanocomposite structure. The hardness values ranged from 11 to 20 Gpa depending on the deposition technique and the amount of the soft a-C(:H) phase present in the sample. The tribological properties of all the coatings were remarkably good when the carbon content was approximately 50 at.%. The formation of a lubricating sp^2-rich C tribofilm between the ball and coating during the pin-on-disk tests was observed by Raman spectroscopy. The tribofilm formed preferentially on the samples prepared by HiPIMS, which had higher C contents. At 750 °C, the degradation of the NbC phases resulted in the formation of an additional a-C phase and niobium oxides.

Keywords

Physical Vapor Deposition; Sputtering; Nanocomposites; Nb–C Films; HiPIMS

1. Introduction

Diamond-like carbon (DLC) is a form of amorphous carbon with a certain quantity of sp^3- hybridized bonds [1,2]. DLC films are well known for their excellent properties, including high hardness, high wear resistance, chemical inertness, and biocompatibility [3]. Some drawbacks of DLC films are their high residual internal stress, poor thermal stability, and low adherence to metallic substrates [4]. Accepted methods for improving these properties include metal doping (Ti, W, Nb, Cr, etc.) [5–8] and incorporation in multilayer films or nanocomposites.

Among the various nanocomposite systems, numerous studies have focused on TiN, WC, and CrC crystals embedded in amorphous and hydrogenated amorphous carbon films [6,9–11] for tribological applications and electrical contacts. Niobium carbide (NbC) is known to exhibit a high melting point, high conductivity, and excellent chemical stability [12,13], making it suitable for electrical components [14], high-temperature environments [15], and biomedical applications [16,17]. NbC thin films have been deposited by plasma-assisted physical vapor deposition (PVD) techniques, including filtered cathodic vacuum arc deposition [18], plasma ion implantation [19], non-reactive magnetron sputtering of Nb and C targets [14], and reactive magnetron sputtering using a hydrocarbon gas as a carbon precursor (CH_4 [7,16,20–22] and C_2H_2 [23,24]). However, NbC thin films obtained using high-energy PVD techniques have been less studied. Most recently, Nb–DLC systems were deposited using hybrid pulsed direct current magnetron sputtering (DC-MS) and high-power magnetron sputtering [25]. High-power impulse magnetron sputtering (HiPIMS) is a variation of conventional DC-MS. This deposition technique is based on the application of short pulses (~100 μs) with a high power density (up to several kW/cm^2) to the sputtering target. This results in a higher ionization degree of the plasma species, which in turn causes densification and a change in the properties of the deposited thin films [26–28].

Sala *et al.* [29] performed a preliminary comparison of NbC thin films prepared by DC-MS and HiPIMS. In this work, the chemical composition, microstructure, morphology, thermal stability, and tribomechanical properties of NbC films were studied to reveal the interrelations between them.

2. Materials and methods

Nb–C coatings were deposited using an industrial CemeCon CC800/9 ML magnetron sputtering machine in DC-MS or HiPIMS mode. The coatings were labeled #DC or #Hi according to the sputtering technique employed (DC-MS or HiPIMS, respectively). Graphite and Nb targets from CemeCon (99.95% purity) were used to deposit the NbC coatings on single-crystalline silicon wafers (100) and mirror-polished cold-worked AISI D2 and SS316 steel substrates. Argon was used for plasma formation, and acetylene was used as a reactive gas to increase the carbon content in specific samples. The background pressure was 3×10^{-3} Pa, and the working pressure was 0.3–0.45 Pa. A DC bias of 120 V was applied to the substrates during the entire deposition process. The sputtering powers were 3.5–3.6 kW and 1.1–1.2 kW for the Nb and C targets, respectively. The HiPIMS pulse parameters were as follows: a duty cycle of 28%, duration of 70 μs, and repetition frequency of 4000 Hz. To improve coating adhesion, a thin layer of pure Nb was initially deposited. Subsequently, the graphite target was switched on for the deposition of the NbC layers according to the deposition parameters summarized in Table 1. A third layer was deposited in samples #2DC, #3Hi, and #4Hi by introducing acetylene at a flow rate of 35 sccm as the reactive gas for the sputtering process of the Nb and C targets. For sample #4Hi, an extra layer of carbon was added by reducing the power applied to the Nb target to 0.3 kW during the last 75 min of the process. Further details about the synthesis procedure and characteristics of the films can be found elsewhere [29].

The chemical compositions of the coatings were measured using electron probe microanalysis (EPMA, JEOL JXA-8200 SuperProbe). The cross sections and top surfaces of the samples were analyzed on silicon substrates by scanning electron microscopy (SEM, Hitachi S4800 and S5200) using a field-emission gun operating at 5 kV. The coating thickness was measured using SEM. For atomic force microscopy (AFM) observations, an atomic force microscope (Nano-Observer CSInstruments) with silicon N-type tips (μmasch) was used in contact mode with the coatings prepared on silicon substrates. X-ray diffraction (XRD, Panalytical Empyrean coupled with a PIXcel Medipix 3 detector) analysis was conducted using a Cu K_α source in the Bragg–Brentano configuration. The NbC crystallite size was estimated from the (111) reflection at 34.7° using the Scherrer equation. Grazing incidence X-ray diffraction (GIXRD, Panalytical Empyrean) analysis was conducted using Cu K_α radiation at an incident angle of 1°. Raman measurements (200–1200 cm^{-1}) of the coated D2 steels were performed using a LabRAM Horiba Jobin Yvon spectrometer equipped with a charge-coupled device (CCD) detector and a diode-pumped solid-state laser (532 nm) operating at 5 mW. All measurements were recorded using a 50× magnification objective and a 100 μm pinhole with a laser exposure of 150 s. The fitting of the D and G Raman bands were performed using Lorentzian functions. The hardness of the films was measured by nanoindentation using a NanoIndenter XP (MTS) system fitted with a Berkovich diamond tip. A CSM pin-on-disk tribometer was used in the rotary mode to perform all measurements on the coated D2 steels, and a 100Cr6 steel ball with a diameter of 6 mm was used. The testing conditions were a linear velocity of 10 cm/s, an applied load of 5 N, 10000 laps, a circumference radius of 3 or 4 mm, a temperature between 20 and 25 °C, and a relative humidity of 40% to 50% in ambient air. Selected samples were subjected to thermal annealing up to 1000 °C at a heating rate of 30 °C/min in an Ar flow (40 mL/min). Once the set point was attained, the temperature was maintained for 60 min before cooling to room temperature.

3. Results and discussion

3.1. Chemical composition

The elemental chemical compositions of the NbC coatings obtained by EPMA are shown in Fig. 1a. Depending on the synthesis conditions, the carbon content varied from 12 to 66 at.%, and the niobium content varied from 29 to 83 at.%. The number of oxygen impurities was relatively low (≤ 5 at.%), except for in coating #3Hi (~10 at.%). Similar oxygen contents (2–11 at.%) can be found in earlier studies [16,17]. The amount of oxygen can be attributed to the oxygen absorbed by the coating during synthesis (residual gases) and exposure to an open atmosphere [30]. Fig. 1b shows the C/Nb ratios of the prepared coatings. In the #1DC sample, the amount of carbon was very low compared to that of niobium because of the synthesis conditions (non-reactive mode).

After the acetylene precursor was introduced in the process, the carbon content increased considerably, up to ~1.1 in samples #2DC and #3Hi. The sample with the highest percentage of carbon was #4Hi (C/Nb > 2) because an extra hydrocarbon layer was deposited on top of the third layer.

3.2. Microstructure

Figure 2 shows secondary electron (SE, left) and backscattered electron (BSE, middle) SEM images of the cross sections of the deposited coatings and as well as top-view (right) images of the samples. Several microstructures were observed corresponding to different sequences of stacked layers. Table 1 shows the coating thickness for each layer measured using SEM and the calculated growth rate. The first layer of coating #1DC (Nb adhesion layer) was approximately 500 nm thick, which changed into a denser structure when carbon was incorporated in the second stage. Coating #2DC exhibited a three-layer structure, in which the additional top layer was generated by the introduction of acetylene as a

carbon precursor. The top layer had a more columnar structure. It is worth noting that the HiPIMS samples developed a clear columnar morphology from the substrate interface to the top surface. Samples #3Hi and #4Hi had very similar microstructures, but sample #4Hi had an extra carbon-rich top layer, which can be clearly observed in the BSE-SEM images. From the top view, samples #1DC and #2DC present considerably more compact structures than those of the HiPIMS samples. The degree of definition of the columnar boundaries increases in the sequence #1DC < #2DC < #3Hi < #4Hi.

Figure 3 displays AFM topographic images (5 × 5 μm^2) of the Nb–C coatings. The columnar growth of the coatings resulted in an increase in the surface roughness. The estimated mean average (Ra) and root mean square (RMS) roughness values of the coatings are shown in Fig. 4. In good agreement with the SEM observations, the DC-MS samples had smoother surfaces than those of the HiPIMS samples. The selected HiPIMS conditions appear to favor more columnar and less compact structures with increased roughness.

3.3. Phase composition

The crystallographic structure of the coatings was previously analyzed by XRD in a conventional coupled Bragg–Brentano configuration [29]. Asymmetric and broad peaks were observed, indicating nanocrystallinity and lattice defects. In this study, GIXRD diffractograms were analyzed to minimize the substrate effect and to gain more information about the top layer. The following JCPDS diffraction charts were used to identify the crystalline phases present in the samples: 34-0370 (Nb), 71-4649 (Fe), 38-1364 (NbC), and 19-0870 (Nb_2C). Fig. 5a shows the diffractograms measured under the conventional (θ–2θ) and grazing incidence angle (1°) configurations. The dominant peaks in the coupled θ–2θ diffractograms are the Fe and Nb peaks,which were due to the steel substrate and the Nb

adhesion layer, respectively. Different phases (either Nb_2C or NbC) formed in the films, depending on the carbon content and sputtering process.

Figure 5b shows a magnified view of the region of the diffractograms where the main peaks were detected (31°–43°). The diffractogram of #1DC was primarily due to the Nb adhesion layer and the top layer of Nb_2C, which was promoted by the incorporation of carbon. Sample #2DC, where acetylene was used as an extra source of carbon, showed very similar phases to those in #1DC, with an additional top layer that was richer in carbon and identified as crystalline NbC. However, sample #3Hi, which was prepared following the same stacking sequence as that of #2DC but via HiPIMS, showed a very different result from the DC-MS samples. In the coupled configuration, the cubic form of niobium carbide (NbC) was identified instead of hexagonal Nb_2C. It has been reported that with the HiPIMS technique, the density of the plasma and the number of ionized species are higher than those in the conventional DC-MS [31,32]. This could favor the incorporation of carbon into the films because of the increased population of C^+ and the assistance of Ar^+ ions present in the high-density plasma. The resulting increase in the C/Nb ratio could lead to the formation of NbC instead of Nb_2C. The #Hi4 sample did not exhibit significant crystallographic differences from #Hi3, indicating that the additional a-C:H top layer was essentially amorphous. The crystal size decreased from 14 nm (sample #2D) to 8 and 9 nm for the HiPIMS samples (#3Hi and #4Hi, respectively).

Figure 6 shows the Raman spectra of the as-deposited coatings. The spectra were measured under identical conditions to allow a direct comparison of their intensities. Disordered graphite can be observed in the Raman spectra with two bands located at approximately 1580–1600 cm^{-1} (G) and 1350 cm^{-1} (D), which can be attributed to the stretching of sp^2 C–C bonds and the breathing mode of sp^2 C–C

aromatic rings, respectively [33]. The Nb–C coating with the lowest carbon content (#1DC) did not present the characteristic D–G bands, indicating the absence of segregated a-C. The presence of disordered carbon was nevertheless confirmed in the remaining coatings, for which the D and G peaks were clearly observed. Significant peak narrowing and an increase in intensity were observed for sample #4Hi owing to the top carbon-rich layer. Comparing samples #2DC and #3Hi, which had similar carbon contents (approximately 45 at.%), HiPIMS promoted the formation of a-C(:H) more than DC-MS.

To obtain complementary information about the carbon structure and chemical bonding, the G- band position, intensity ratio between the D and G peaks (ID/IG), and G-peak width (GFWHM) were determined from the Raman spectra, as shown in Fig. 7. According to Ferrari and Robertson [33], the features of these Raman peaks allow the classification of samples in transition between nanocrystalline graphite and disordered carbon, with a predominance of sp2 bonding. Samples #2DC and #3Hi had very similar Raman spectra, exhibiting broad D and G bands typically observed in a-C films. Similar ID/IG ratios (1.2 to 1.5) were found for NbC-based nanocomposites prepared by reactive magnetron sputtering [23,24]. Sample #4Hi, with a G peak at 1600 cm-1, a small GFWHM value, and an ID/IG ratio of ~0.9, is in agreement with region 1 of the three-stage model, representing the transition from bulk to nanocrystalline graphite [1]. This may be attributed to the final top C-rich layer that was grown only on this sample, which generated a more ordered graphitic structure. Fig. 8 schematically summarizes the different structures and compositions of the prepared coatings based on the XRD, GIXRD, SEM, AFM, and Raman spectroscopy characterization results.

3.4. Mechanical properties

The film hardness and reduced Young's modulus values are presented in Fig. 9. The hardness varied

between 11 and 20 GPa, in good agreement with the values presented by Nedfors *et al.* for NbC_x-based coatings (16–23 GPa) [34]. The reduced Young's modulus did not vary significantly among the samples (~220 GPa). The samples prepared by DC-MS had higher hardness values (18–20 GPa) than those of the samples prepared by HiPIMS (11–12 GPa). Comparing #2DC and #3Hi, which had similar carbon contents (~50 at.%) and stacking layer sequence, the sample prepared by HiPIMS had a lower hardness. This can be attributed to the higher fraction of amorphous carbon, as shown in the Raman spectra, and less crystalline structure, as determined by the decrease in crystalline size estimated by Scherrer's equation. A similar decrease in hardness was observed for NbC_x thin films prepared by reactive and non- reactive PVD as a function of the C/Nb ratio [24].

3.5. Tribological properties

Figure 10 displays representative friction curves for the four different coatings. Except for #1DC, the Nb–C samples exhibited low and steady friction coefficient (μ) values of approximately 0.25. For sample #DC1, the friction coefficient curve increased suddenly to 1 after a short initial running-in period. Subsequent tests on this sample always led to the same behavior, which is consistent with strong adhesive ball–film interactions, film delamination, or cracking failure. As determined by Raman spectroscopy, this coating did not have amorphous carbon phase.

Therefore, the top surface was essentially a layer of a hard metal carbide. The use of a metal ball for the tribological test resulted in strong metal-to-metal bonding, which increased the adhesion forces at the film interface and caused the sudden rise in the coefficient of friction [35]. The variation at the beginning of the test could be due to polishing of the sample because it had some initial roughness. Fig. 11 summarizes the average measured friction coefficients and estimated ball and coating wear rates. No significant variations were observed in the tribological properties($\mu \approx 0.25$, and $k \approx 10^{-6}$ mm^3/Nm)

except for sample #1DC, which failed prematurely. A deeper investigation of the friction mechanism was conducted through Raman spectroscopy of the ball scars and coating wear tracks.

3.6. Raman analysis of the friction contact regions

Figure 12 shows the worn ball surface and wear track of sample #1DC together with the corresponding Raman spectra. The wear was relatively small because the test was stopped after a sudden increase in the friction coefficient. The Raman spectra of the material adhered to the ball had two broad bands between 650 and 850 cm^{-1} associated with Nb and Fe oxides from the coating [36] and the ball, respectively. The presence of free amorphous carbon in metal carbide/a-C nanocomposites allows the formation of a lubricant layer between the ball and the coating, decreasing friction and excessive wear [6,37]. The absence of a free amorphous carbon in this sample, as evidenced by Raman spectroscopy, explains the sudden increase in the friction coefficient and the failure of the film.

The Raman spectra of various positions on the wear track of the #2DC sample were similar to those of the as-deposited state (Track P1) and other colored zones, indicating the presence of oxides (Track P2). On the ball scar, (Ball P1), analysis of debris outside the worn area provided evidence of graphitization of the original disordered carbon phase of the coating. The D and G bands could be clearly identified and were even more pronounced than those of the original sample. In the center of the ball (Ball P2), no transfer material was identified, indicating that it was not present or that it was too thin to be detected (Fig. 13).

The black spots observed on the wear track of the #3Hi sample (Fig. 14) appear to indicate that some local delamination occurred during the test. However, the corresponding Raman spectra were consistent with the presence of amorphous carbon at all positions. On the ball scar, an increase in the

carbon content was observed together with some poorly formed FeO_x/NbO_x oxides at approximately 650 and 850 cm^{-1} [38–40].

The Raman spectra of the wear track of sample #4Hi and the ball scar (Fig. 15) indicate that the nanocrystalline graphite initially present in the film transformed into more disordered carbon during the test. This sp^2-rich layer on both counterfaces lubricated the contact, which reduced the friction coefficient and wear rates of the ball and track. Oxides were observed only in small regions on the top of the ball.

3.7. Thermal stability and oxidation resistance

To obtain further insight into the two types of coatings with similar carbon contents but prepared by different methods, samples #2DC and #3Hi underwent further thermal behavior and oxidation resistance analysis. Fig. 16 shows the Raman spectra of both samples after thermal treatment at 500, 750, and 1000 °C in an argon atmosphere. Niobium oxides and carbon were the main phases identified during the successive annealing treatments. NbO_2 and Nb_2O_5 are denoted by the presence of two double bands at approximately 280 and 650 cm^{-1} and a narrow peak at 920 cm^{-1}, as shown by Cao *et al.* and Kreissl *et al.* [40,41]. The formation of amorphous carbon was confirmed by the presence of the two characteristic D and G peaks of sp^2 bonds of disordered carbon at 1350 and 1585 cm^{-1}, respectively. The D and G bands became more intense and defined, and the G-peak position shifted toward higher wavenumbers as the temperature increased to 750 °C. These transformations are indicative of an increased presence of free carbon and increased clustering of the sp^2 carbon phase. At 500 °C, none of the coatings showed clear signs of oxidation, but at 750 °C, the spectra diverged owing to their different thermal stabilities. Coating #2DC developed a smooth band at 670 cm^{-1}, which is associated with the formation of Nb–O bonds, while maintaining the D and G doublet. An optical

micrograph of the surface did not reveal significant surface modifications. However, the #3Hi sample had a heterogeneous surface (as shown in the optical micrograph), on which various spots were detected. Analysis of these different areas indicated that they had a different degree of oxidation compared with the that of the surrounding areas. The spectrum obtained from these spots indicated the carbonaceous phase disappeared, while the niobium oxide bands centered at 280 and 650 cm^{-1} were enhanced. Furthermore, the spectrum of the surrounding areas was very similar to that of #2DC, indicating that oxidation progressed to a minor extent. When the samples were subjected to thermal annealing at 1000 °C, the peaks originating from the niobium oxides (NbO_2 and/or Nb_2O_5) and the silicon substrate at 520 cm^{-1} were clearly identified, indicating the total oxidation of the coating [40,42,43]. The total disappearance of the carbon bands at 1000 °C can be explained by the formation of volatile CO_2. Oxidation of the samples could originate from oxygen and water impurities in the tubular furnace or the film composition. The #3Hi sample had the lowest threshold temperature for the onset of oxidation, and the localized oxidation (pitting) can be correlated with the columnar microstructure, which allowed inward diffusion of oxygen through the open intercolumnar boundaries.

Figure 17a shows the evolution of the diffractograms with increasing thermal annealing treatment temperature (500, 700, and 1000 °C) for the #2DC sample in argon. The main crystalline phases identified for the pristine sample were Nb, Nb_2C, and NbC (as shown in detail in Fig. 5a and 5b). The diffractogram at 500 °C shows the presence of the NbC phase and a growing Nb_2C phase, which could be formed by partial decomposition of the cubic NbC phase. Differences in thermal stability and oxidation resistance can be observed at 750 °C. At this temperature, the initial NbC coating of #2DC began to transform into one of the multiple Nb_2O_5 polymorphic forms, specifically the TT phase (JCPDS #28-0317) [44]. It is believed that the high relative intensity of this new phase made it difficult to

distinguish the remaining NbC nanocrystals. At 1000 °C, the niobium atoms were completely oxidized, and H-Nb2O5 (JCPDS #32-0711), which is the most thermodynamically stable niobium oxide phase at atmospheric pressure, became the predominant phase [44].

Figure 17b shows the diffractograms of sample #3Hi after thermal treatment at the same temperatures (500, 750, and 1000 °C) in argon. The main phases identified for the pristine sample were Nb and NbC (as shown in detail in Fig. 5a and 5b). When the sample was heated to 500 °C, a new phase, Nb_2C, was detected, which was probably due to the loss of carbon in the sample (as shown by Raman spectroscopy). The diffractograms of the sample annealed at 750 °C indicate the presence of the TT-Nb_2O_5 phase and a new NbO_2 phase not detected in sample #2DC. It is believed that this NbO_2 phase transformed into the most stable high-temperature and oxidized phase (H- Nb_2O_5) when the sample was heated to 1000 °C. Similar phase transformations have been found in WC/a-C and TiBC/a-C nanocomposite coatings, where the samples did not show significant signs of degradation and maintained an almost unaltered structure [45,46]. At 750 °C, the degradation of the TiB_xC_y and WC phases proceeded by the formation of an additional a-C phase and metal oxides.

4. Conclusions

Nanostructured Nb–C coatings with various contents of nanocrystalline niobium, niobium carbides, and amorphous hydrogenated carbon phases were prepared with a controlled architecture and phase composition via DC-MS and HiPIMS. The obtained coatings exhibited significant differences in their structure, chemical bonding, and tribomechanical properties as a function of the carbon content. The coatings deposited by HiPIMS developed a considerably more columnar structure comprising nanocrystalline Nb and NbC (vs. Nb_2C that formed under DC-MS) in conjunction with a higher amount

of a-C(:H). These features could be related to the higher carbon and argon ionization under the high-power impulse conditions, which favors a higher incorporation of carbon atoms. Nevertheless, these changes did not necessarily improve the mechanical properties (approximately 11–12 GPa), thermal stability, and oxidation resistance (< 750 °C) owing to the marked columnar growth and open porosity. Regarding the tribological properties, both sets of coatings (DC-MS and HiPIMS) demonstrated protective behavior ($\mu \approx 0.25$, and $k \approx 10^{-7}$ mm^3/Nm) when the carbon content was above 50 at.%, which allowed the formation of a lubricating sp^2-rich C tribofilm in the contact area. The thermal stability was improved by a more compact structure, which helped to stabilize the niobium carbide phases and increased the oxidation resistance. In summary, these results highlight the importance of film compactness, disrupting the columnar growth, and/or decreasing the intercolumnar distance for enhancing the mechanical properties and oxidation resistance of Nb–C coatings. The use of HiPIMS technology does not necessarily improve the film microstructure and functionality.

Rather, the plasma conditions must be optimized to select an appropriate ion bombardment (type, energy, and flux) to guarantee film densification.

Acknowledgments

This research was supported by the La Caixa Foundation, Secretaria d'Universitats i Recerca (SUR) del Departament d'Empresa i Coneixement (DEC) de la Generalitat de Catalunya, and Fons Socials Europeus [2019FI_B01190, 2020FI_B100114].

References

[1] C. Casiraghi, A.C. Ferrari, J. Robertson, Raman spectroscopy of hydrogenated amorphous carbons, Phys. Rev. B - Condens. Matter Mater. Phys. 72 (2005) 1–14. https://doi.org/10.1103/PhysRevB.72.085401.

[2] A.C. Ferrari, J. Robertson, Interpretation of Raman spectra of disordered and amorphous carbon, Phys. Rev. Bical Rev. 61 (1999). https://doi.org/10.1063/1.2219983.

[3] J. Robertson, Properties of diamond-like carbon, Surf. Coatings Technol. 50 (1992) 185–203. https://doi.org/10.1016/0257-8972(92)90001-Q.

[4] S. Zhang, H. Xie, X. Zeng, P. Hing, Residual stress characterization of diamond-like carbon coatings by an X-ray diffraction method, Surf. Coatings Technol. 122 (1999) 219–224. https://doi.org/10.1016/S0257-8972(99)00298-4.

[5] D. Martínez-Martínez, C. López-Cartes, A. Fernández, J.C. Sánchez-López, Influence of the microstructure on the mechanical and tribological behavior of TiC/a-C nanocomposite coatings, Thin Solid Films. 517 (2009) 1662–1671. https://doi.org/10.1016/j.tsf.2008.09.091.

[6] J.C. Sánchez-López, D. Martínez-Martínez, M.D. Abad, A. Fernández, Metal carbide/amorphous C-based nanocomposite coatings for tribological applications, Surf. Coatings Technol. 204 (2009) 947–954. https://doi.org/10.1016/j.surfcoat.2009.05.038.

[7] C.N. Zoita, L. Braic, A. Kiss, M. Braic, Characterization of NbC coatings deposited by magnetron sputtering method, Surf. Coatings Technol. 204 (2010) 2002–2005. https://doi.org/10.1016/j.surfcoat.2009.08.050.

[8] X. Sui, J. Liu, S. Zhang, J. Yang, J. Hao, Microstructure, mechanical and tribological characterization of CrN/DLC/Cr-DLC multilayer coating with improved adhesive wear resistance, Appl. Surf. Sci. 439 (2018) 24–32. https://doi.org/10.1016/j.apsusc.2017.12.266.

[9] M.D. Abad, J.C. Sánchez-López, M. Brizuela, A. García-Luis, D. V. Shtansky, Influence of carbon chemical bonding on the tribological behavior of sputtered nanocomposite TiBC/a- C coatings, Thin Solid Films. 518 (2010) 5546–5552. https://doi.org/10.1016/j.tsf.2010.04.038.

[10] K. Nygren, M. Samuelsson, A. Flink, H. Ljungcrantz, Å. Kassman Rudolphi, U. Jansson, Growth and characterization of chromium carbide films deposited by high rate reactive magnetron sputtering for electrical contact applications, Surf. Coatings Technol. 260 (2014) 326–334. https://doi.org/10.1016/j.surfcoat.2014.06.069.

[11] M. Colasuonno, T.C. Rojas, A. Patelli, S. Dominguez-Meister, M. Bazzan, J.C. Sánchez- López, Tribological properties of TiC/a-C:H nanocomposite coatings prepared via HiPIMS, Appl. Surf. Sci. 440 (2018) 458–466. https://doi.org/10.1016/j.apsusc.2018.01.135.

[12] M. Cuppari, S. Santos, Physical Properties of the NbC Carbide, Metals (Basel). 6 (2016) 250. https://doi.org/10.3390/met6100250.

[13] T. Amriou, B. Bouhafs, H. Aourag, B. Khelifa, S. Bresson, C. Mathieu, FP-LAPW investigations of electronic structure and bonding mechanism of NbC and NbN compounds, Phys. B Condens. Matter. 325 (2003) 46–56. https://doi.org/10.1016/S0921-4526(02)01429-1.

[14] L. Yate, L. Emerson Coy, G. Wang, M. Beltrán, Tailoring mechanical properties and electrical conductivity of flexible niobium carbide nanocomposite thin films, RSC Adv. 4 (2014) 61355–61362. https://doi.org/10.1039/c4ra11292j.

[15] B. Sustarsic, M. Jenko, M. Godec, L. Kosec, Microstructural investigation of NbC-doped vacuum-sintered tool-steel-based composites, User Model. User-Adapt. Interact. 71 (2003) 77–82. https://doi.org/10.1016/S0042-207X(02)00717-0.

[16] M. Braic, V. Braic, M. Balaceanu, A. Vladescu, C.N. Zoita, I. Titorencu, V. Jinga, F. Miculescu, Preparation and characterization of biocompatible Nb-C coatings, Thin Solid Films. 519 (2011) 4064–4068. https://doi.org/10.1016/j.tsf.2011.01.193.

[17] L. Yate, L.E. Coy, D. Gregurec, W. Aperador, S.E. Moya, G. Wang, Nb-C nanocomposite films with enhanced biocompatibility and mechanical properties for hard-tissue implant applications, ACS Appl. Mater. Interfaces. 7 (2015) 6351–6358. https://doi.org/10.1021/acsami.5b01193.

[18] A. Bendavid, P.J. Martin, T.J. Kinder, E.W. Preston, The deposition of NbN and NbC thin films by filtered vacuum cathodic arc deposition, Surf. Coatings Technol. 163–164 (2003) 347–352. https://doi.org/10.1016/S0257-8972(02)00623-0.

[19] Y.Y. Chang, D.Y. Wang, W. Te Wu, Tribological enhancement of CrN coatings by niobium and carbon ion implantation, Surf. Coatings Technol. 177–178 (2004) 441–446. https://doi.org/10.1016/j.surfcoat.2003.09.022.

[20] K. Zhang, S.X. Du, P. Ren, C.Q. Hu, W.T. Zheng, M. Wen, Preparation and Microstructure, Mechanical, Tribological Properties of Niobium Carbide Films, Mater. Sci. Forum. 898 (2017) 1498–1504. https://doi.org/10.4028/www.scientific.net/msf.898.1498.

[21] K. Zhang, M. Wen, G. Cheng, X. Li, Reactive magnetron sputtering deposition and characterization of niobium carbide films, Vacuum. 99 (2014) 233–241. https://doi.org/10.1016/j.vacuum.2013.06.012.

[22] K. Zhang, M. Wen, Q.N. Meng, C.Q. Hu, X. Li, C. Liu, W.T. Zheng, Effects of substrate bias voltage on the microstructure, mechanical properties and tribological behavior of reactive sputtered niobium carbide films, Surf. Coatings Technol. 212 (2012) 185–191. https://doi.org/10.1016/j.surfcoat.2012.09.046.

[23] N. Nedfors, O. Tengstrand, E. Lewin, A. Furlan, P. Eklund, L. Hultman, U. Jansson, Structural, mechanical and electrical-contact properties of nanocrystalline-NbC/amorphous- C coatings deposited by magnetron sputtering, Surf. Coatings Technol. 206 (2011) 354–359. https://doi.org/10.1016/j.surfcoat.2011.07.021.

[24] N. Nedfors, O. Tengstrand, A. Flink, A.M. Andersson, Reactive sputtering of NbCx-based

nanocomposite coatings: An up-scaling study, Surf. Coatings Technol. 253 (2014) 100–108. https://doi.org/10.1016/j.surfcoat.2014.05.021.

[25] J.C. Ding, W. Dai, T.F. Zhang, P. Zhao, J.M. Yun, K.H. Kim, Q.M. Wang, Microstructure and properties of Nb-doped diamond-like carbon films deposited by high power impulse magnetron sputtering, Thin Solid Films. 663 (2018) 159–167. https://doi.org/10.1016/j.tsf.2018.07.012.

[26] A. Hecimovic, A.P. Ehiasarian, Spatial and temporal evolution of ion energies in high power impulse magnetron sputtering plasma discharge, J. Appl. Phys. 108 (2010) 3–11. https://doi.org/10.1063/1.3486018.

[27] K. Sarakinos, A. Braun, C. Zilkens, S. Mráz, Exploring the potential of high power impulse magnetron sputtering for growth of diamond-like carbon films, Surf. Coatings Technol. 206 (2012) 2706–2710. https://doi.org/10.1016/j.surfcoat.2011.11.032.

[28] M. Samuelsson, K. Sarakinos, H. Högberg, E. Lewin, U. Jansson, B. Wälivaara, H. Ljungcrantz, U. Helmersson, Growth of Ti-C nanocomposite films by reactive high power impulse magnetron sputtering under industrial conditions, Surf. Coatings Technol. 206 (2012) 2396–2402. https://doi.org/10.1016/j.surfcoat.2011.10.039.

[29] N. Sala, M.D. Abad, J.C. Sánchez-López, M. Cruz, J. Caro, C. Colominas, Tribological performance of Nb-C thin films prepared by DC and HiPIMS, Mater. Lett. 277 (2020) 128334. https://doi.org/10.1016/j.matlet.2020.128334.

[30] P. Kumar, M. Gupta, D.M. Phase, J. Stahn, Influence of oxygen on growth of carbon thin films, AIP Conf. Proc. 1942 (2018). https://doi.org/10.1063/1.5028913.

[31] M. Samuelsson, D. Lundin, K. Sarakinos, F. Björefors, B. Wälivaara, H. Ljungcrantz, U. Helmersson, Influence of ionization degree on film properties when using high power impulse magnetron sputtering, J. Vac. Sci. Technol. A Vacuum, Surfaces, Film. 30 (2012) 031507. https://doi.org/10.1116/1.3700227.

[32] J.T. Gudmundsson, N. Brenning, D. Lundin, U. Helmersson, High power impulse magnetron sputtering discharge, J. Vac. Sci. &Technology. A. Vacuum, Surfaces, Film. (2012).

[33] A.C. Ferrari, J. Robertson, Interpretation of Raman spectra of disordrred and amorphous carbon, Phys. Rev. B. 61 (2000) 14 295.

[34] N. Nedfors, O. Tengstrand, A. Flink, A.M. Andersson, P. Eklund, L. Hultman, U. Jansson, Reactive sputtering of NbCx-based nanocomposite coatings: An up-scaling study, Surf. Coatings Technol. 253 (2014) 100–108. https://doi.org/10.1016/j.surfcoat.2014.05.021.

[35] L. Tang, C. Gao, J. Huang, H. Zhang, W. Chang, Dry sliding friction and wear behaviour of hardened AISI D2 tool steel with different hardness levels, Tribol. Int. 66 (2013) 165–173. https://doi.org/10.1016/j.triboint.2013.05.006.

[36] A. Mcconnell, C.R.N. Rao, Raman spectra of niobium oxides, Spectrochim. Acta. 32 (1976) 1067–1076.

[37] T. Vitu, A. Escudeiro, T. Polcar, A. Cavaleiro, Sliding properties of Zr-DLC coatings: The effect of tribolayer formation, Surf. Coatings Technol. 258 (2014) 734–745. https://doi.org/10.1016/j.surfcoat.2014.08.003.

[38] J.C. Sánchez-López, M.D. Abad, A. Justo, R. Gago, J.L. Endrino, A. García-Luis, M. Brizuela, Phase composition and tribomechanical properties of Ti-B-C nanocomposite coatings prepared by magnetron sputtering, J. Phys. D. Appl. Phys. 45 (2012). https://doi.org/10.1088/0022-3727/45/37/375401.

[39] B. Gunawardana, N. Singhal, P. Swedlund, Degradation of Chlorinated Phenols by Zero. Valent Iron and Bimetals of Iron : A Review, 16 (2011) 187–203.

[40] C. Cao, D. Ford, S. Bishnoi, T. Proslier, B. Albee, E. Hommerding, A. Korczakowski, L. Cooley, G. Ciovati, J.F. Zasadzinski, Detection of surface carbon and hydrocarbons in hot spot regions of niobium superconducting rf cavities by Raman spectroscopy, Phys. Rev. Spec. Top. - Accel. Beams. 16 (2013). https://doi.org/10.1103/PhysRevSTAB.16.064701.

[41] H.T. Kreissl, M.M.J. Li, Y.K. Peng, K. Nakagawa, T.J.N. Hooper, J. V. Hanna, A. Shepherd, T.S. Wu, Y.L. Soo, S.C.E. Tsang, Structural Studies of Bulk to Nanosize Niobium Oxides with Correlation to Their Acidity, J. Am. Chem. Soc. 139 (2017) 12670–12680. https://doi.org/10.1021/jacs.7b06856.

[42] S. Periasamy, S. Venkidusamy, R. Venkatesan, J. Mayandi, J. Pearce, J.H. Selj, R. Veerabahu, Micro-Raman Scattering of Nanoscale Silicon in Amorphous and Porous Silicon, Zeitschrift Fur Phys. Chemie. 231 (2017) 1585–1598. https://doi.org/10.1515/zpch-2016-0961.

[43] J. Aziz, H. Kim, S. Rehman, M.F. Khan, D.K. Kim, Chemical nature of electrode and the switching response of RF-sputtered NBOX films, Nanomaterials. 10 (2020) 1–11. https://doi.org/10.3390/nano10112164.

[44] L. Pan, Y. Wang, X.J. Wang, H.Y. Qu, J.P. Zhao, Y. Li, A. Gavrilyuk, Hydrogen photochromism in Nb2O5 powders, Phys. Chem. Chem. Phys. 16 (2014) 20828–20833. https://doi.org/10.1039/c4cp02834a.

[45] M.D. Abad, S.C. Veldhuis, J.L. Endrino, B.D. Beake, A. García-Luis, M. Brizuela, J.C. Sánchez-López, Mechanical and phase stability of TiBC coatings up to 1000 C, J. Vac. Sci. Technol. A Vacuum, Surfaces Film. 32 (2014). https://doi.org/10.1116/1.4861365.

[46] S. El Mrabet, M.D. Abad, C. López-Cartes, D. Martínez-Martínez, J.C.J.C. Sánchez-López, Thermal evolution of WC/C nanostructured coatings by raman and in situ XRD analysis, Plasma Process. Polym. 6 (2009) 444–449. https://doi.org/10.1002/ppap.200931004.

List of figure captions

Figure 1. (a) Atomic elemental composition and (b) C/Nb ratio of the prepared Nb–C thin films.

Figure 2. Cross-sectional (left, SE; middle, BSE) and top-view (right) SEM images of the Nb–C films.

Figure 3. AFM images of the Nb–C coatings.

Figure 4. Surface roughness values (Ra and Rms) obtained by AFM measurements of the Nb–C coatings.

Figure 5. (a) XRD patterns of the Nb–C coatings deposited under different conditions measured under Bragg–Brentano and grazing incidence angle (1°) configurations; (b) detail of the region of interest.

Figure 6. Raman spectra of the different coatings. Note that the spectra are plotted in counts (not in arbitrary units); thus, the changes in band intensity are significant.

Figure 7. G-peak position, ID/IG ratio, and GFWHM for the samples containing disordered carbon.

Figure 8. Schematics of the Nb–C coatings based on the XRD, GIXRD, SEM, AFM and Raman spectroscopy characterization results.

Figure 9. Hardness and reduced Young's modulus measurements.

Figure 10. Friction coefficient vs. sliding distance for the various coatings.

Figure 11. Friction coefficients and wear rates (ball and disk) for the various coatings.

Figure 12. Optical micrographs of the (a) wear track of coating #1DC and (b) ball wear scar; (c) corresponding Raman analysis of the specified zones.

Figure 13. Optical micrographs of the (a) wear track of coating #2DC and (b) ball wear scar; (c) corresponding Raman analysis of the specified zones.

Figure 14. Optical micrographs of the (a) wear track on coating #3Hi and (b) ball wear scar; (c) corresponding Raman analysis of the specified zones.

Figure 15. Optical micrographs of the (a) wear track of coating #4Hi and (b) ball wear scar; (c) corresponding Raman analysis of the specified zones.

Figure 16. Raman spectra of the (a) #2DC and (b) #3Hi coatings at temperatures up to 1000 °C. Optical micrographs corresponding to some investigated zones are included as examples. Note that the spectra are plotted in counts (not in arbitrary units); thus, the changes in the band intensity are significant.

Figure 17. XRD patterns of the (a) #2DC and (b) #3Hi coatings at temperatures up to 1000 °C.

Table 1 - Sala - R1

Nb-C thin films prepared by DC-MS and HiPIMS: synthesis, structure and tribomechanical properties
N. Sala et al.
Surface and Coatings Technology "VSI:ICMCTF-2021".

Table

Table 1. Deposition conditions, growth rate, and coating thickness for each layer of the various samples.

Film	Sputtering time (min)				Cathode power (kW)		Thickness (nm)				Total Thickness (μm)	Growth rate (nm/min)			
	Nb	Nb+C	Nb+C+ C_2H_2	C+C_2H_2	Nb	C	Nb	Nb+C	Nb+C+ C_2H_2	C+C_2H_2		Nb	Nb+C	Nb+C+ C_2H_2	C+C_2H_2
#1DC	50	35	-	-	3.5	1.1	538	362	-	-	0.90	11	10		-
#2DC	50	45	50	-	3.5	1.1	530	505	694	-	1.73	11	11	14	-
#3Hi	45	40	40	-	3.6	1.2	398	574	654	-	1.63	9	14	16	-
#4Hi	35	35	35	75	3.6	1.2	264	435	495	180	1.37	8	12	14	2

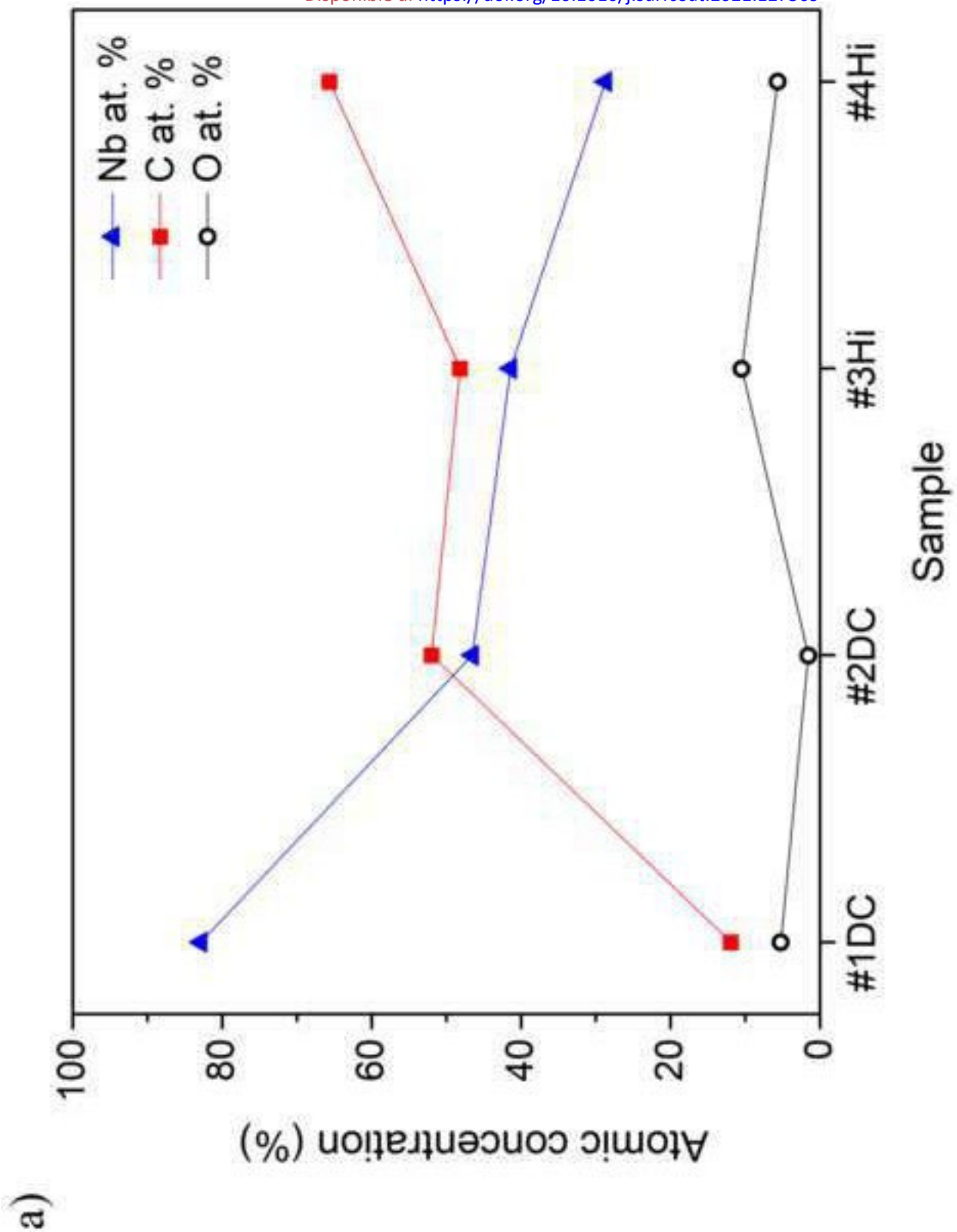

Figure 1a

Figure 1b

Click here to access/download;Figure;Figure 1b.tif

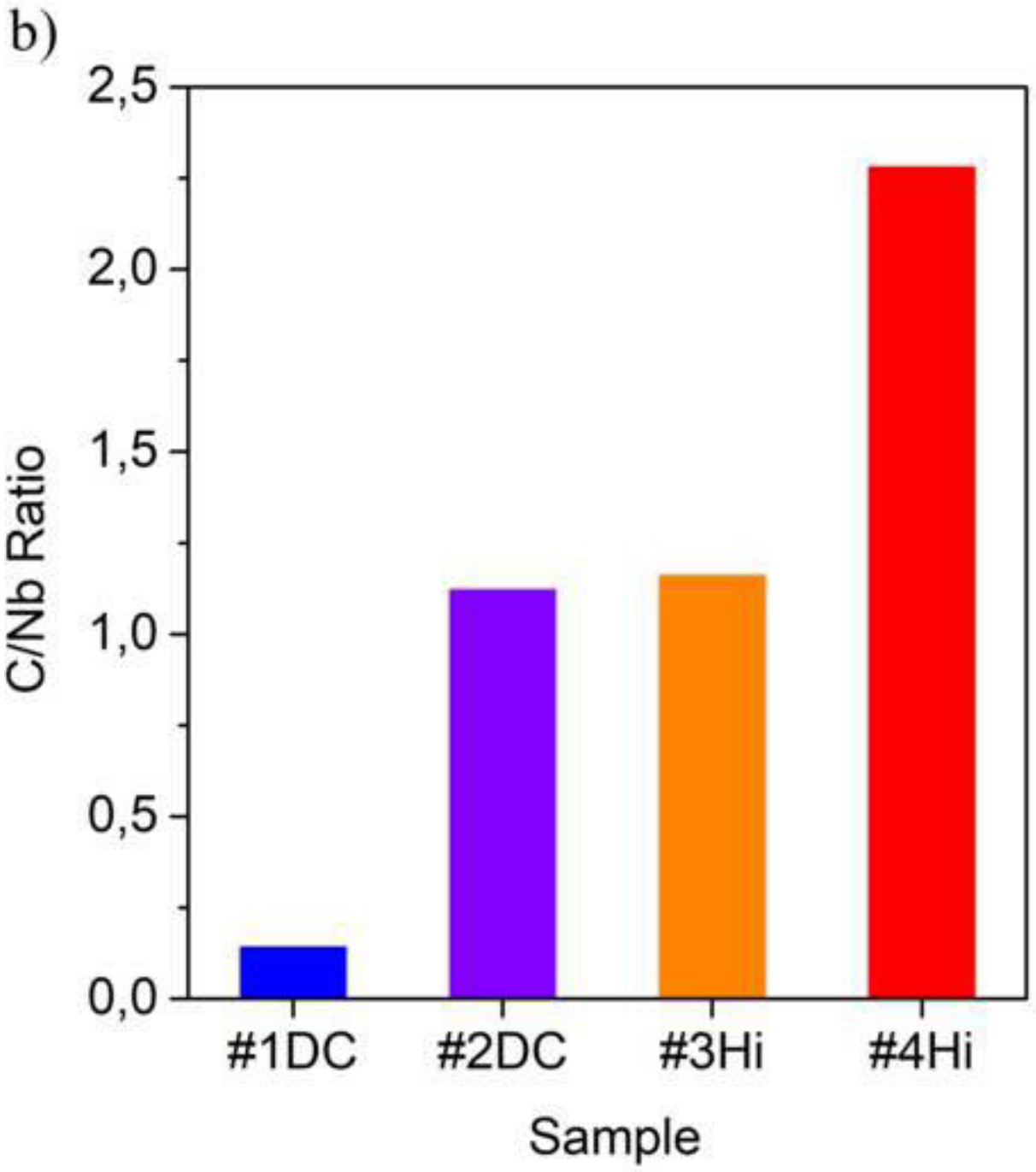

This is a post-print (final draft post-refeering
Published in final edited form as
N. Sala, M. D. Abad, J. C. Sánchez-López, J. Caro, C. Colominas. Nb–C thin films prepared by DC-MS and HiPIMS: Synthesis, structure, and tribomechanical properties. En: *Surface and Coatings Technology.* 2021. Vol.422, p.127569.
Disponible a: https://doi.org/10.1016/j.surfcoat.2021.127569

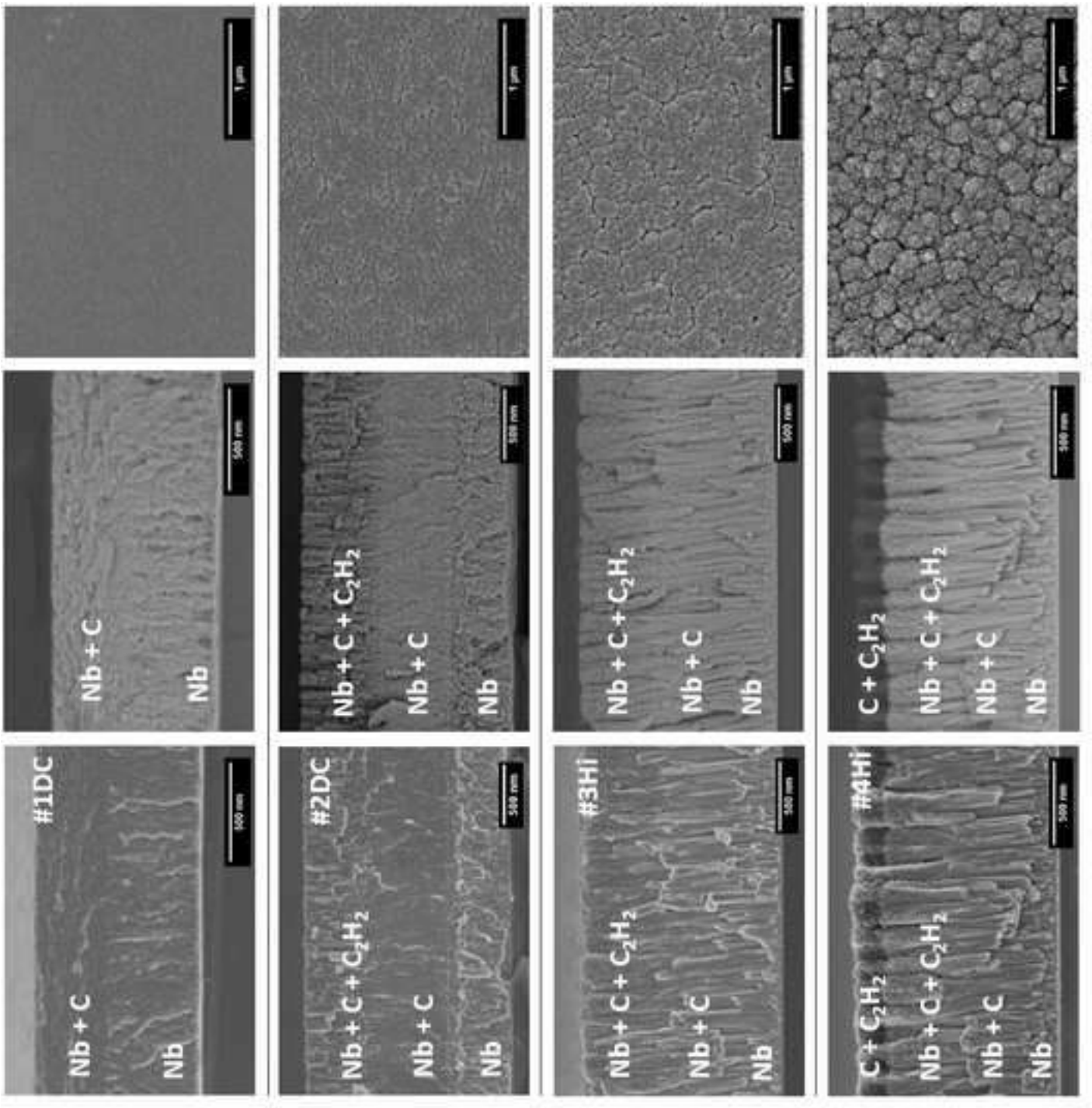

Figure 2 - Sala - R1

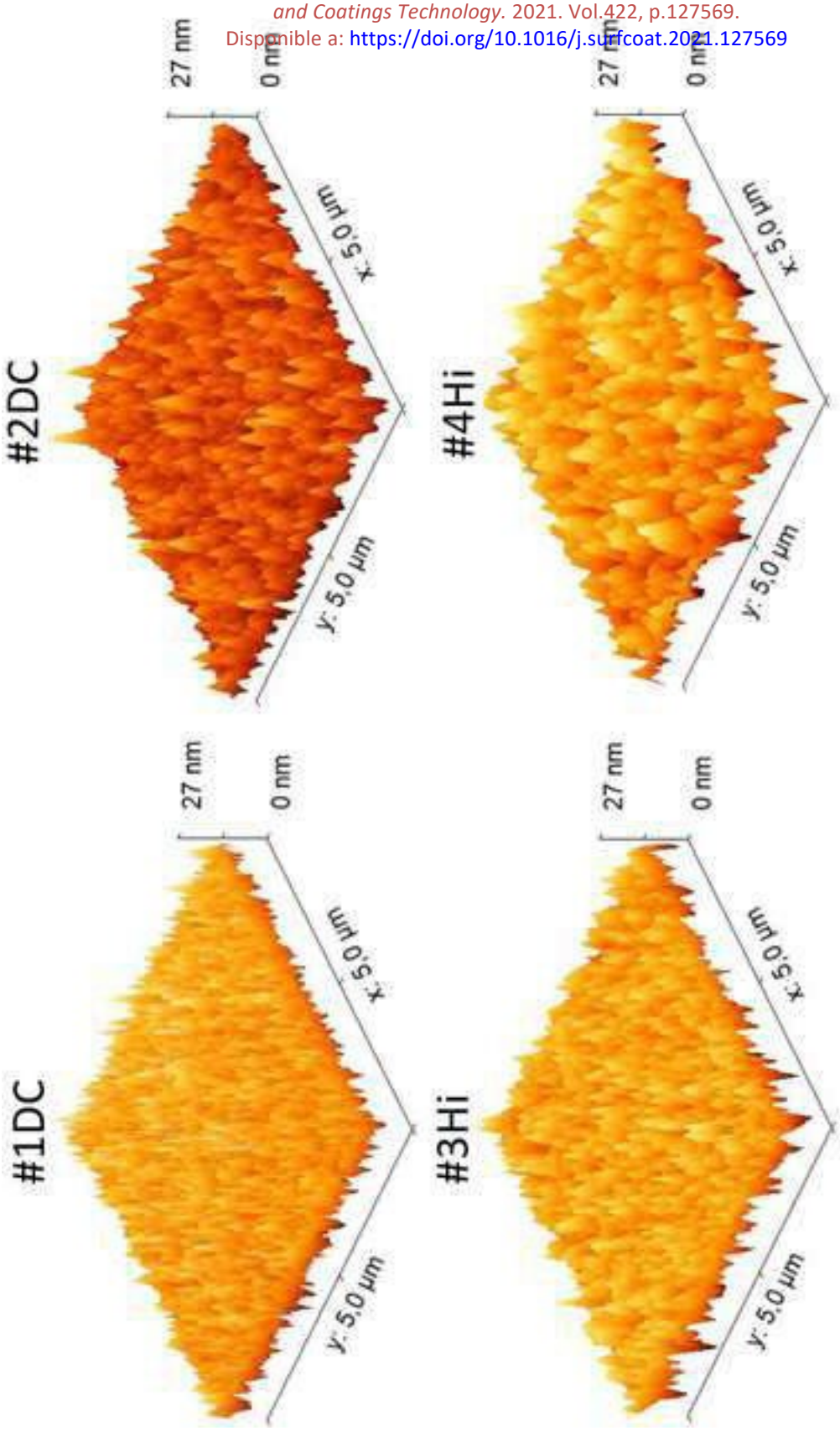

Figure 3

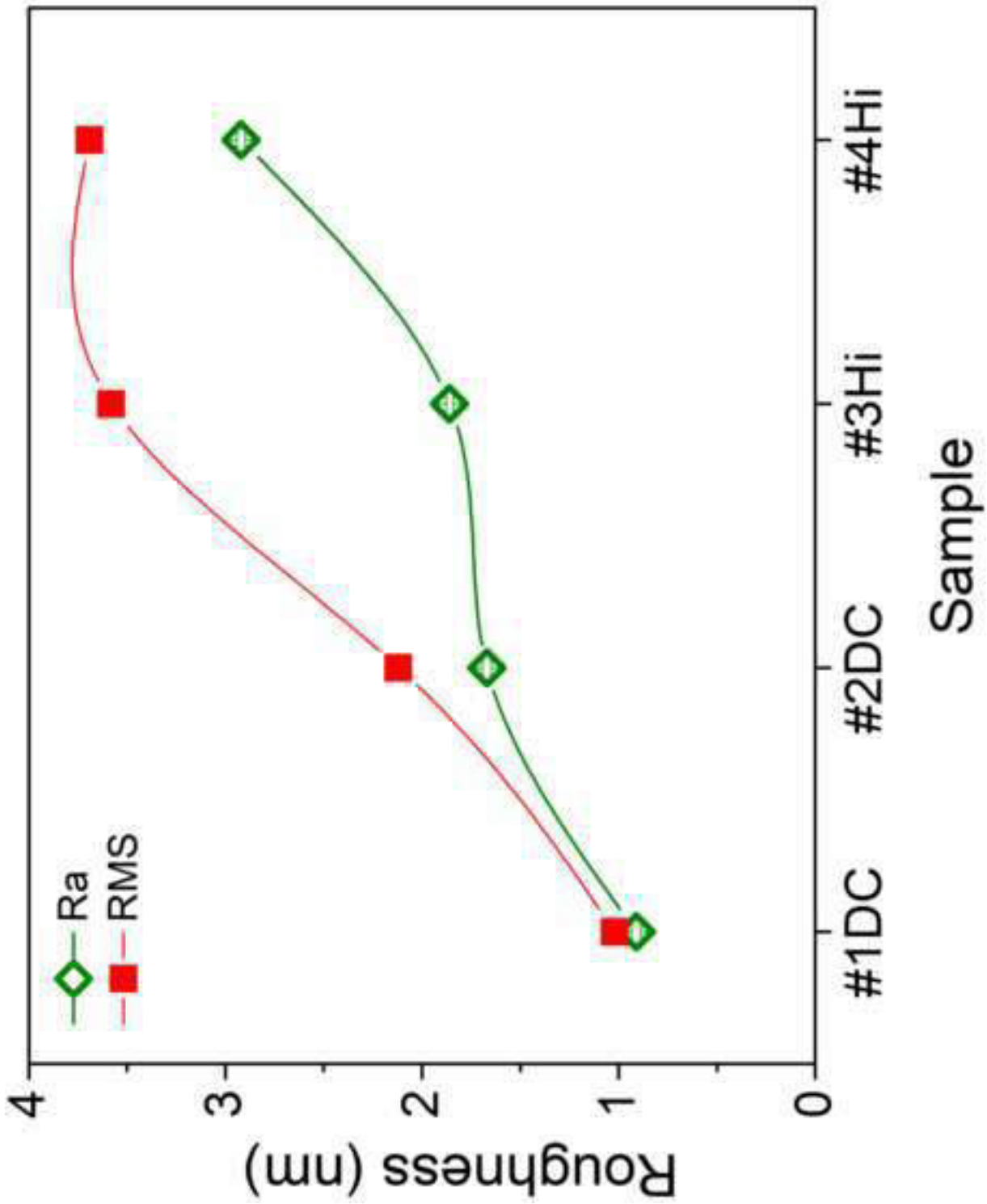

Figure 4

This is a post-print (final draft post-refeering
Published in final edited form as
N. Sala, M. D. Abad, J. C. Sánchez-López, J. Caro, C. Colominas. Nb–C thin films prepared by DC-MS and HiPIMS: Synthesis, structure, and tribomechanical properties. En: *Surface and Coatings Technology.* 2021. Vol.422, p.127569.
Disponible a: https://doi.org/10.1016/j.surfcoat.2021.127569

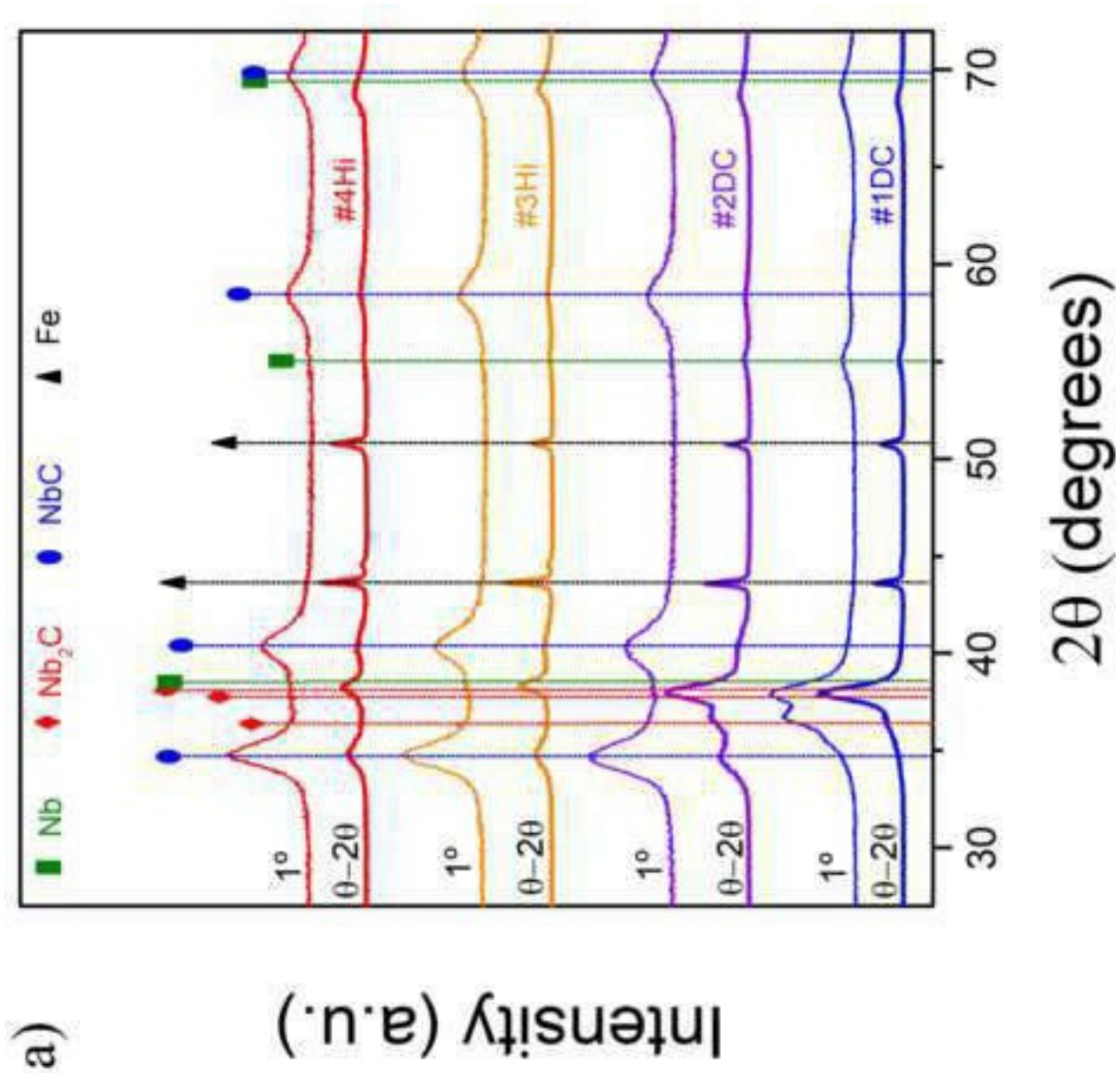

Figure 5a

This is a post-print (final draft post-refeering
Published in final edited form as
N. Sala, M. D. Abad, J. C. Sánchez-López, J. Caro, C. Colominas. Nb–C thin films prepared by DC-MS and HiPIMS: Synthesis, structure, and tribomechanical properties. En: *Surface and Coatings Technology.* 2021. Vol.422, p.127569.
Disponible a: https://doi.org/10.1016/j.surfcoat.2021.127569

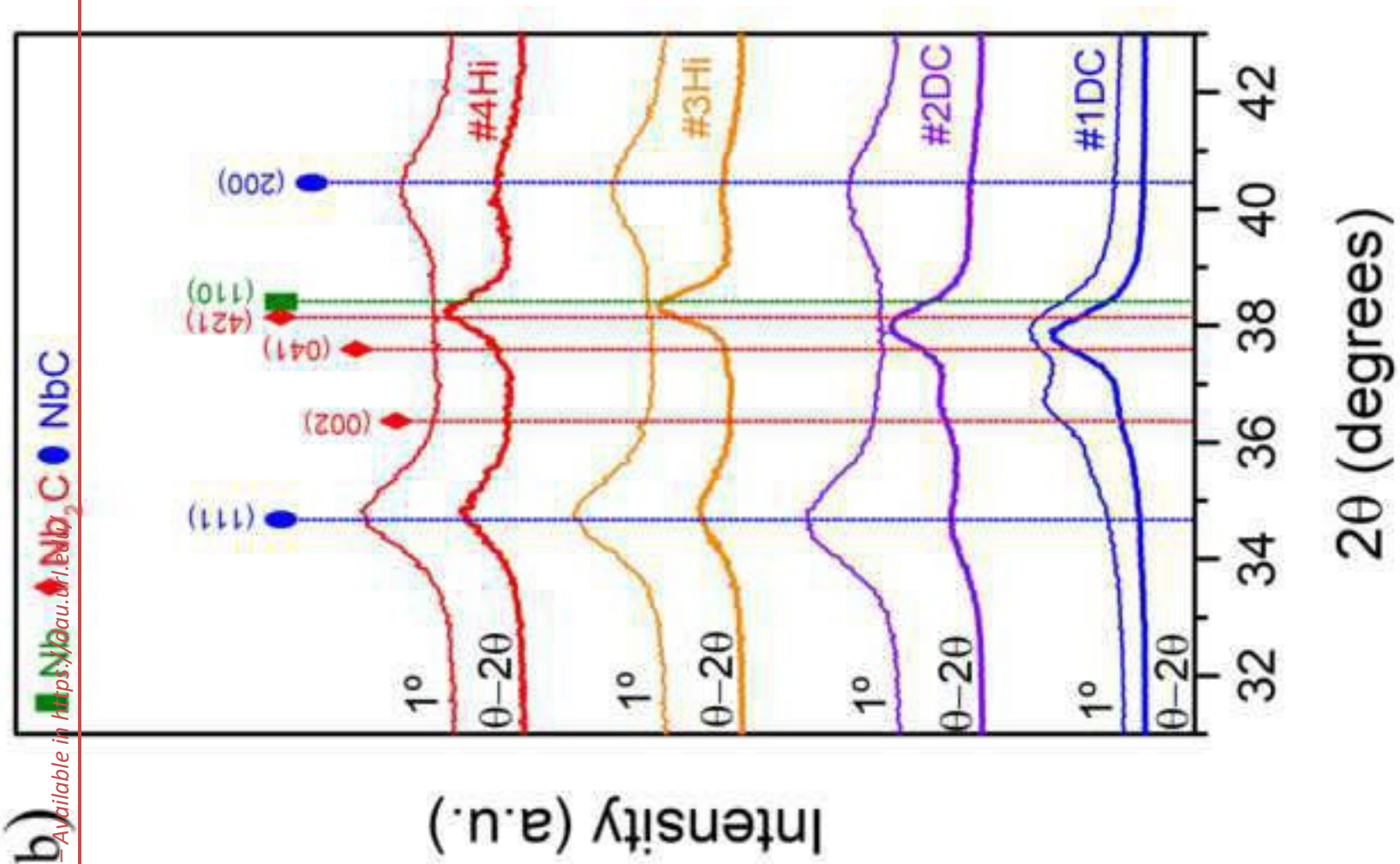

Figure 5b

This is a post-print (final draft post-refeering
Published in final edited form as
N. Sala, M. D. Abad, J. C. Sánchez-López, J. Caro, C. Colominas. Nb–C thin films prepared by DC-MS and HiPIMS: Synthesis, structure, and tribomechanical properties. En: *Surface and Coatings Technology.* 2021. Vol.422, p.127569.
Disponible a: https://doi.org/10.1016/j.surfcoat.2021.127569

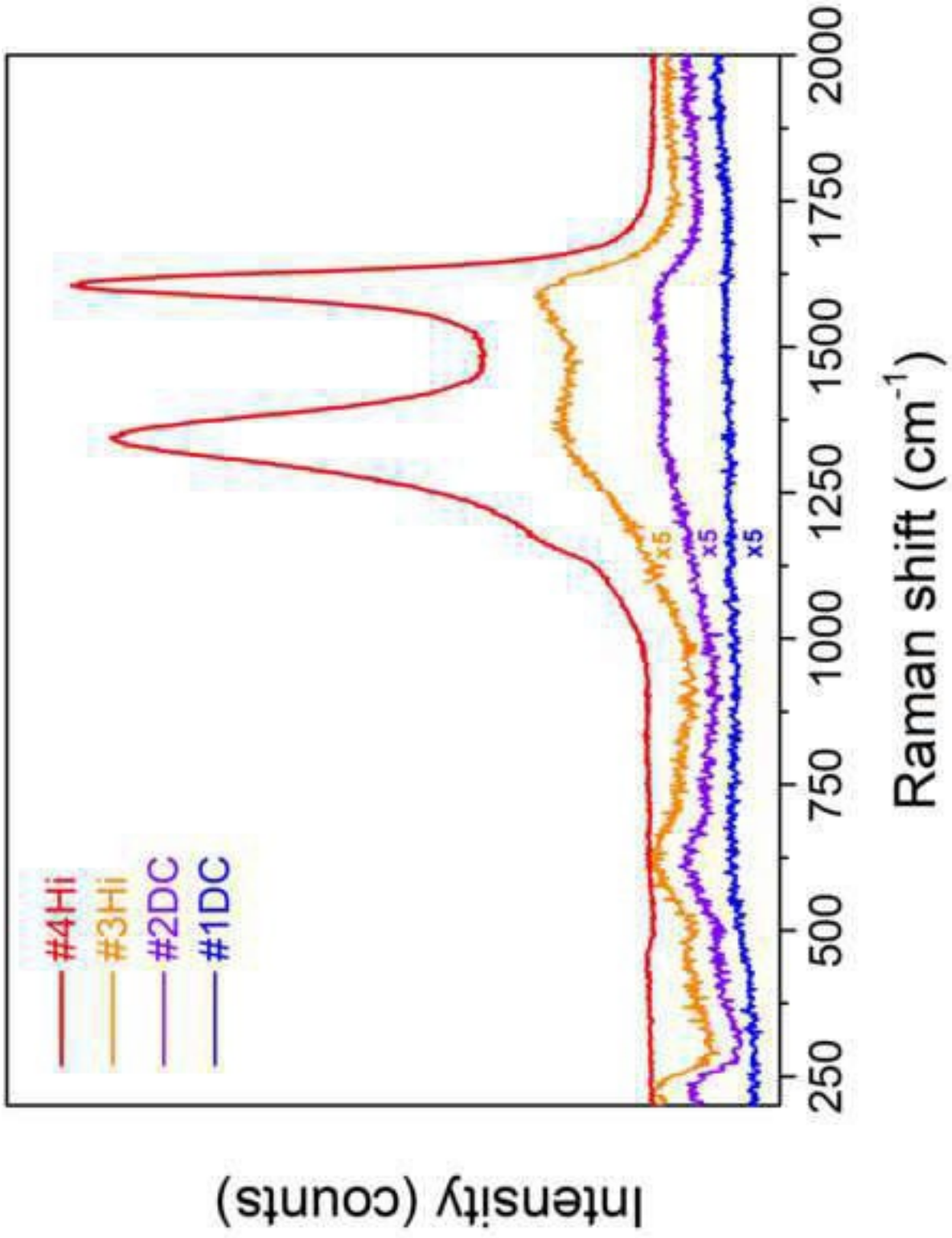

Figure 6

This is a post-print (final draft post-refeering
Published in final edited form as
N. Sala, M. D. Abad, J. C. Sánchez-López, J. Caro, C. Colominas. Nb–C thin films prepared by DC-MS and HiPIMS: Synthesis, structure, and tribomechanical properties. En: *Surface and Coatings Technology*. 2021. Vol.422, p.127569.
Disponible a: https://doi.org/10.1016/j.surfcoat.2021.127569

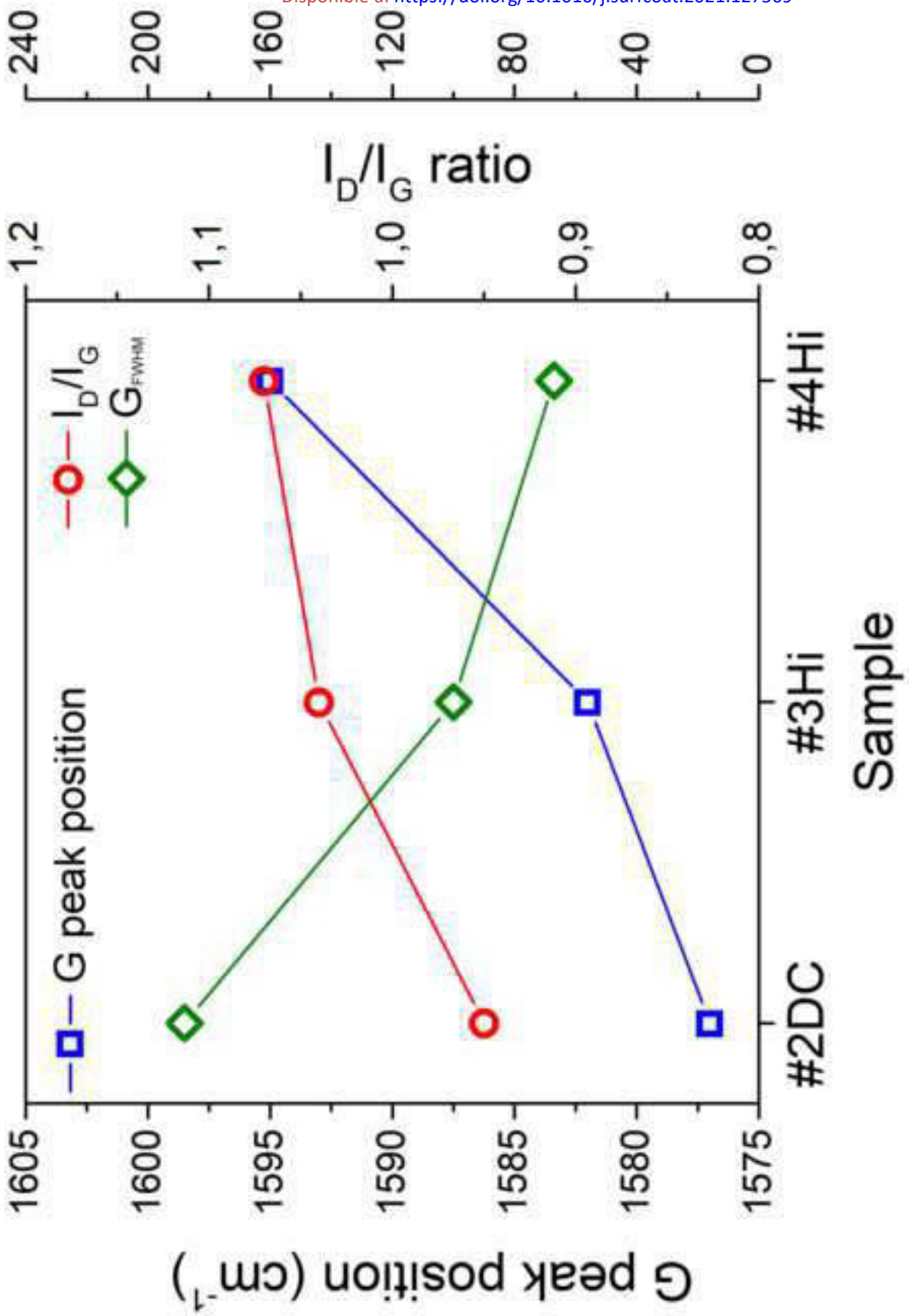

Figure 7 - Sala - ICMCTF21- R2

This is a post-print (final draft post-refeering
Published in final edited form as
N. Sala, M. D. Abad, J. C. Sánchez-López, J. Caro, C. Colominas. Nb–C thin films prepared by DC-MS and HiPIMS: Synthesis, structure, and tribomechanical properties. En: *Surface and Coatings Technology*. 2021. Vol.422, p.127569.
Disponible a: https://doi.org/10.1016/j.surfcoat.2021.127569

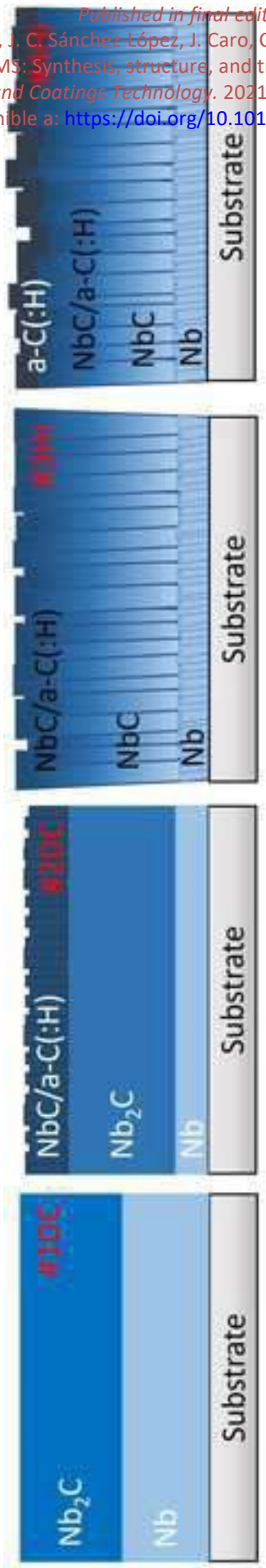

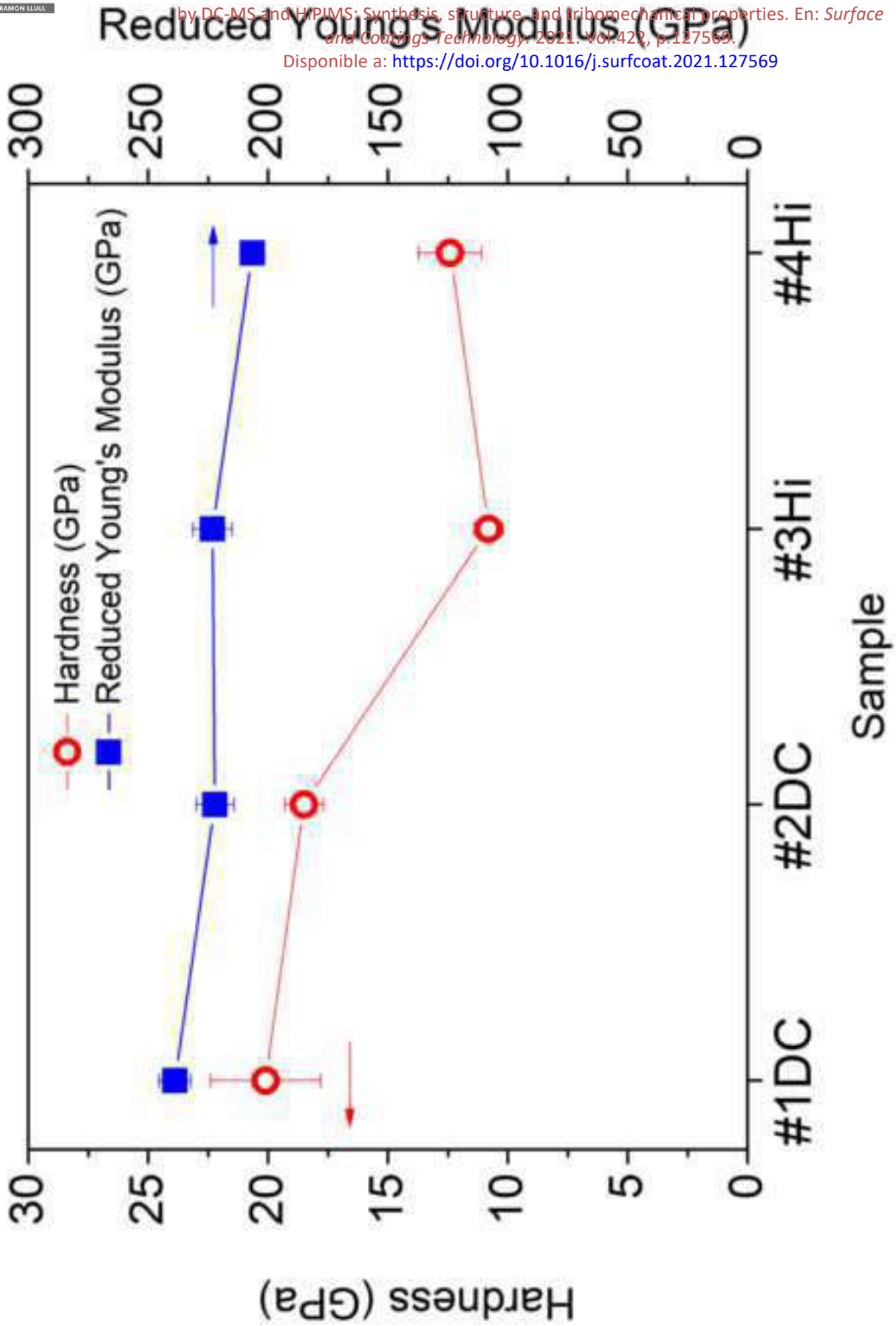

Figure 9

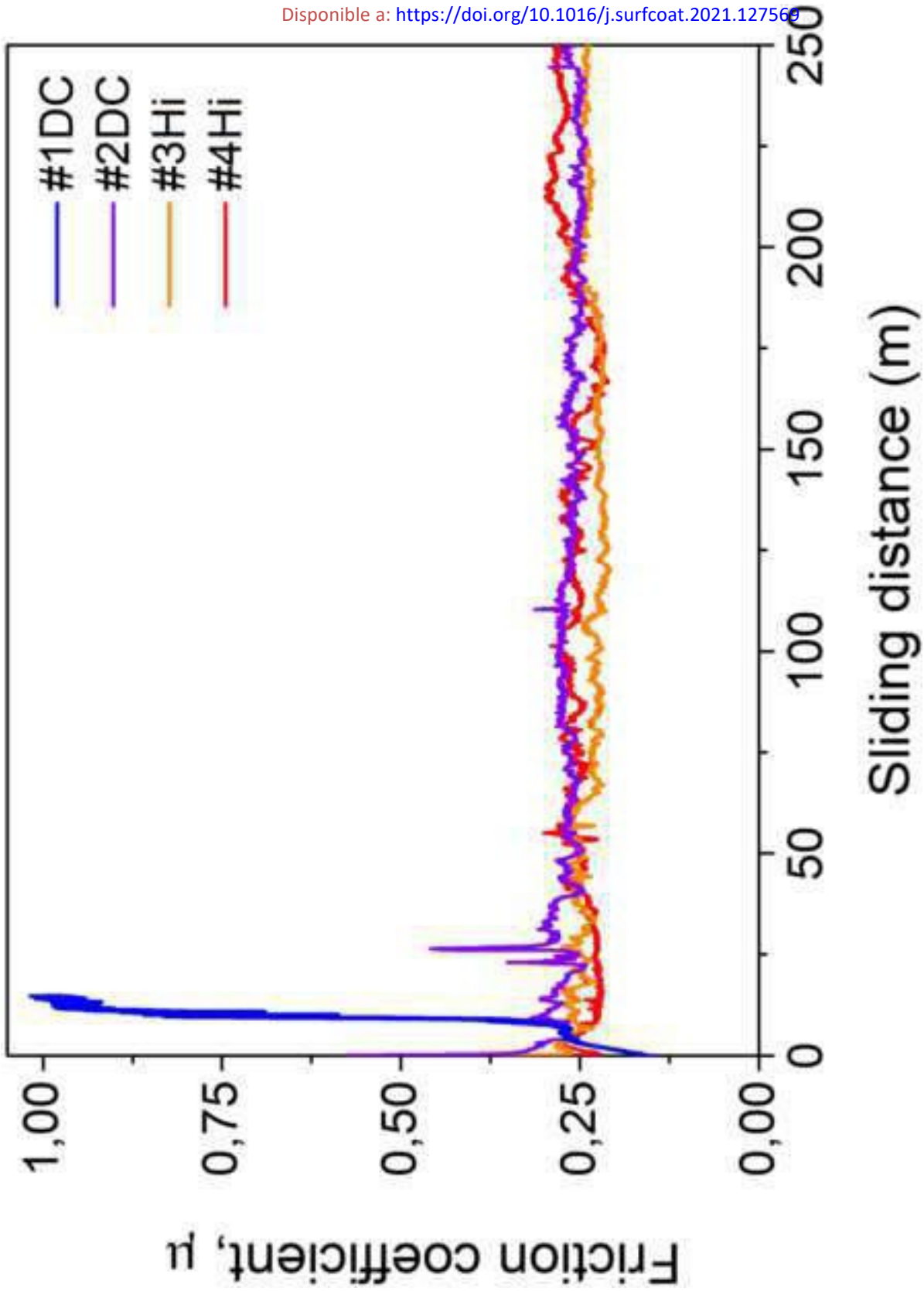

Figure 10

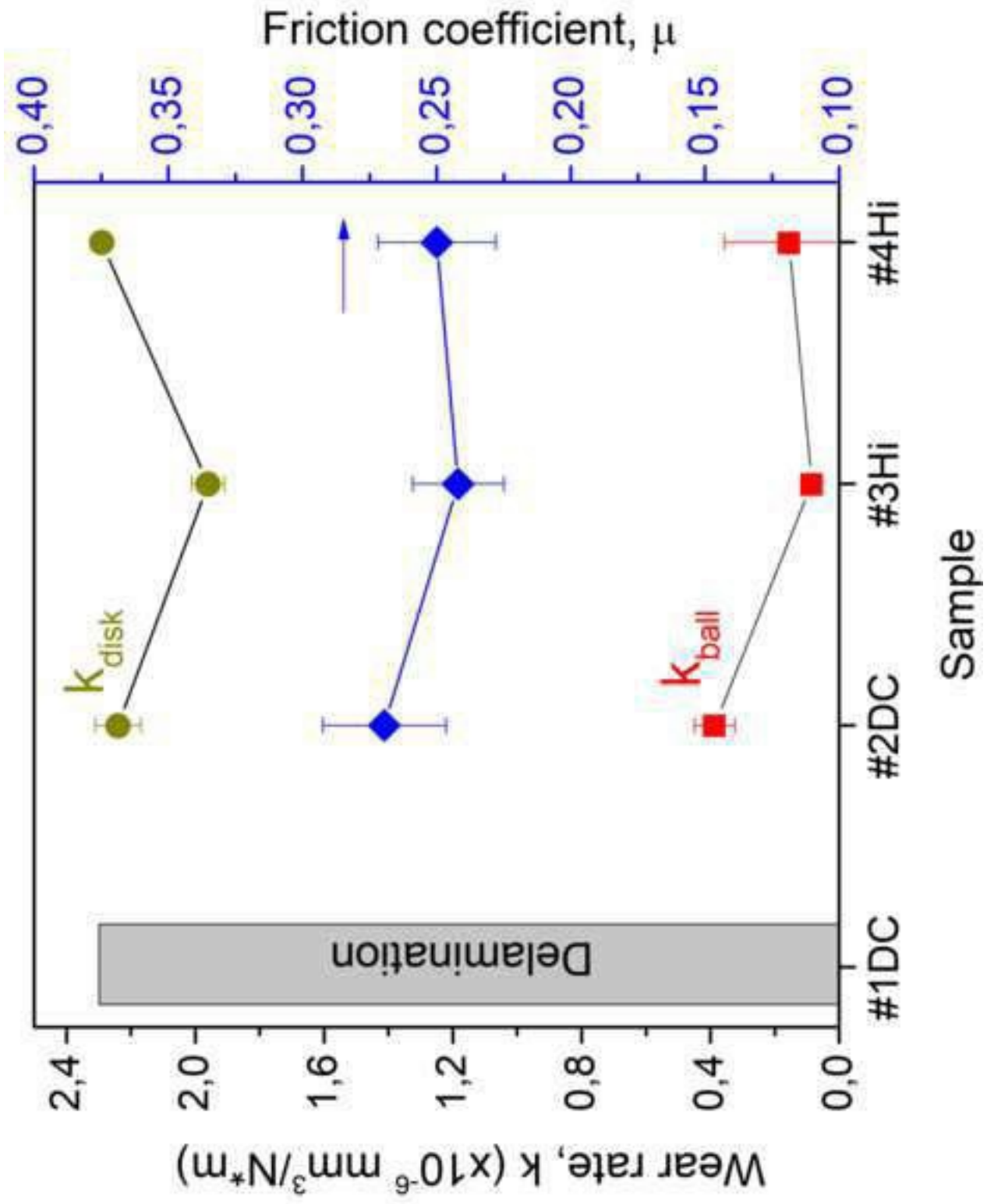

Figure 11

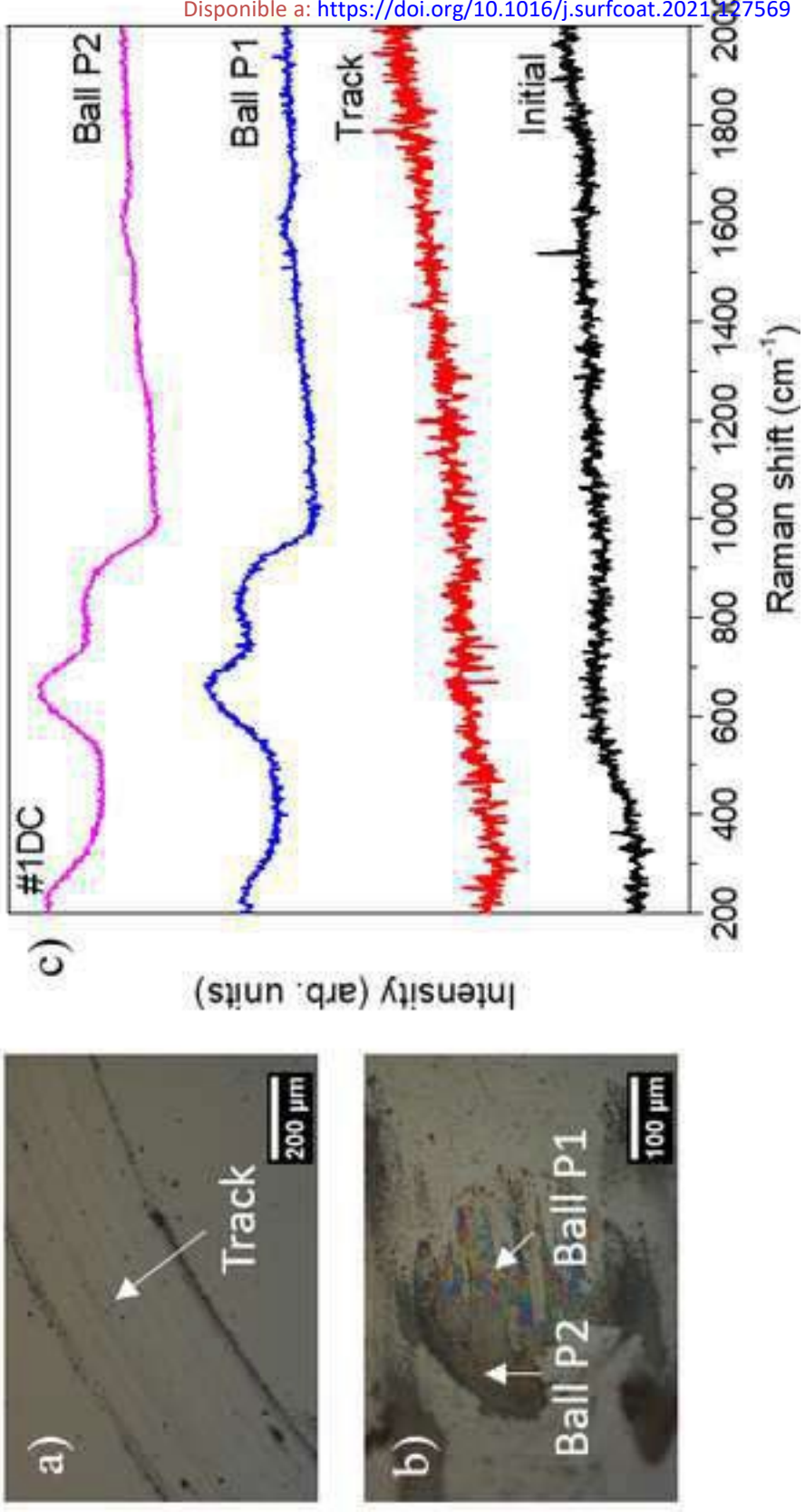

Figure 12

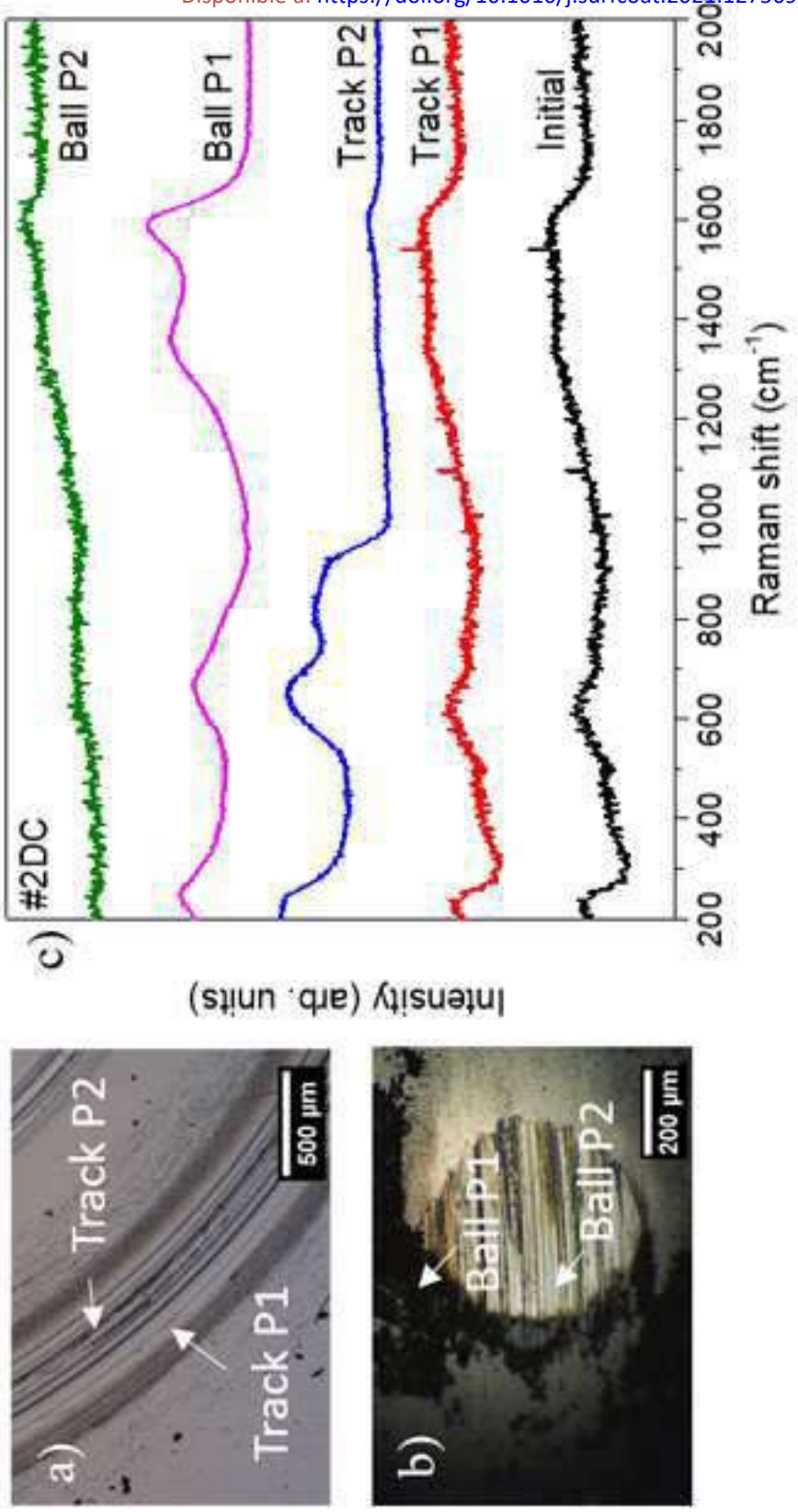

Figure 13

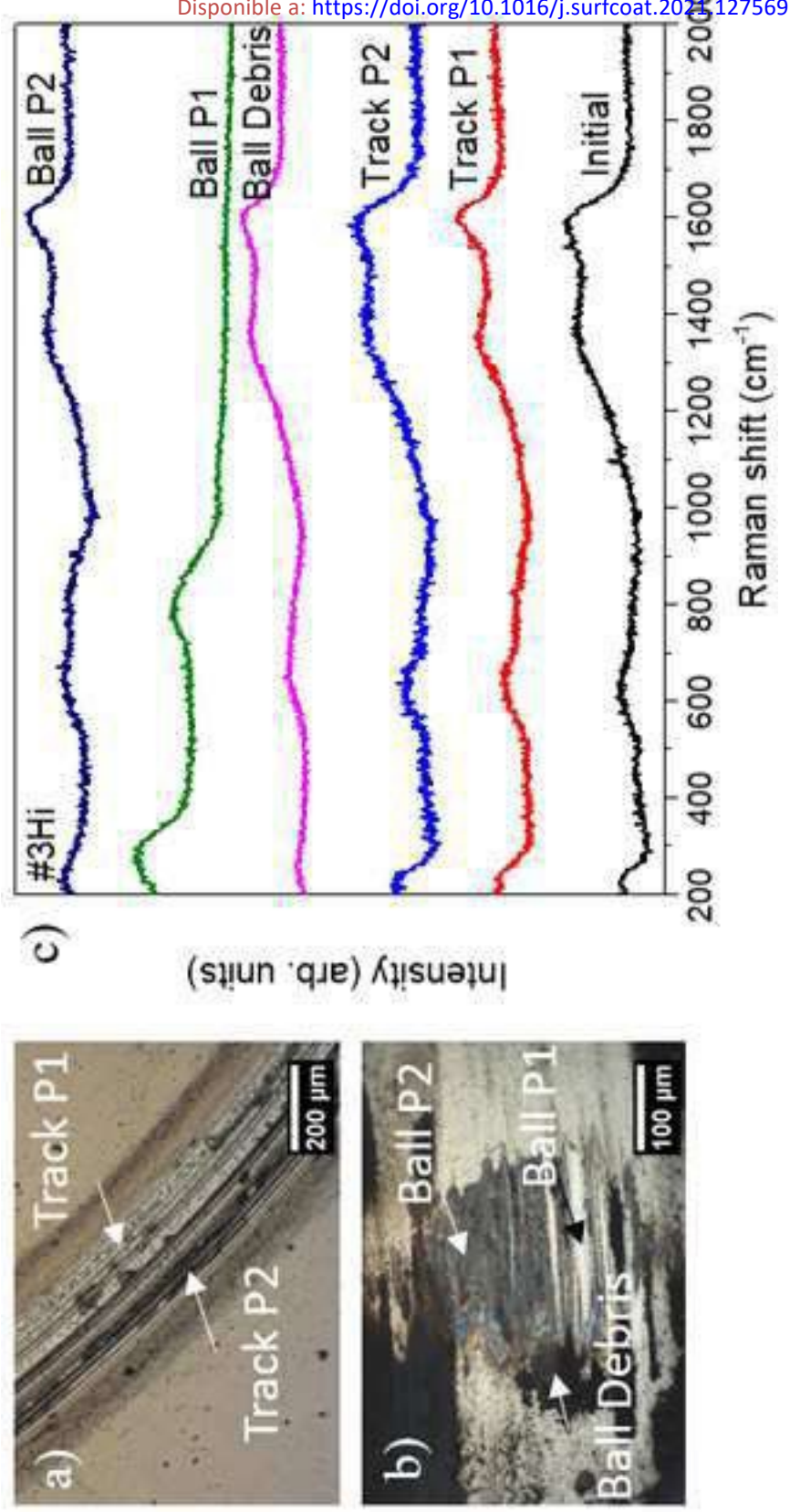

Figure 14

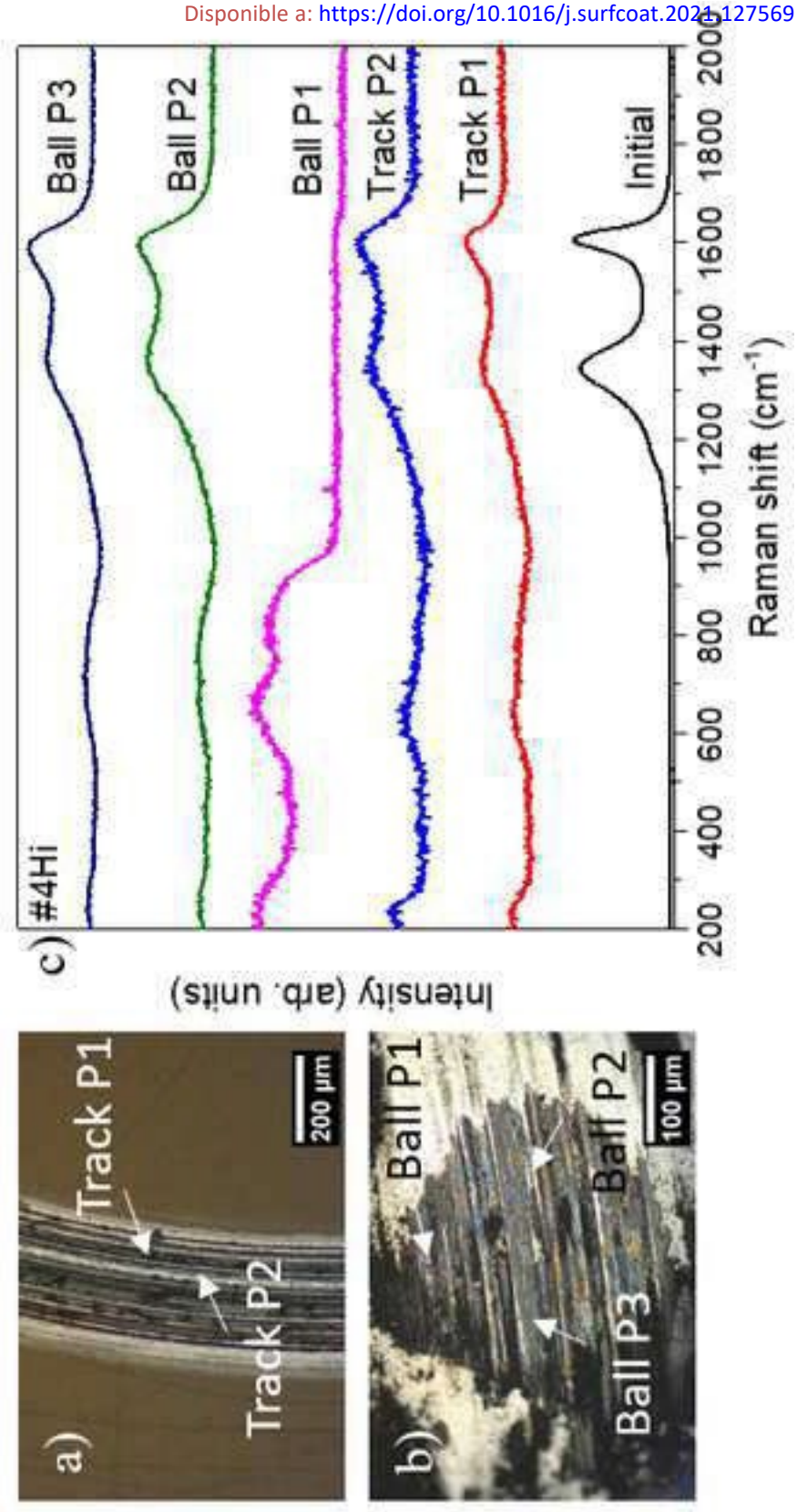

Figure 15

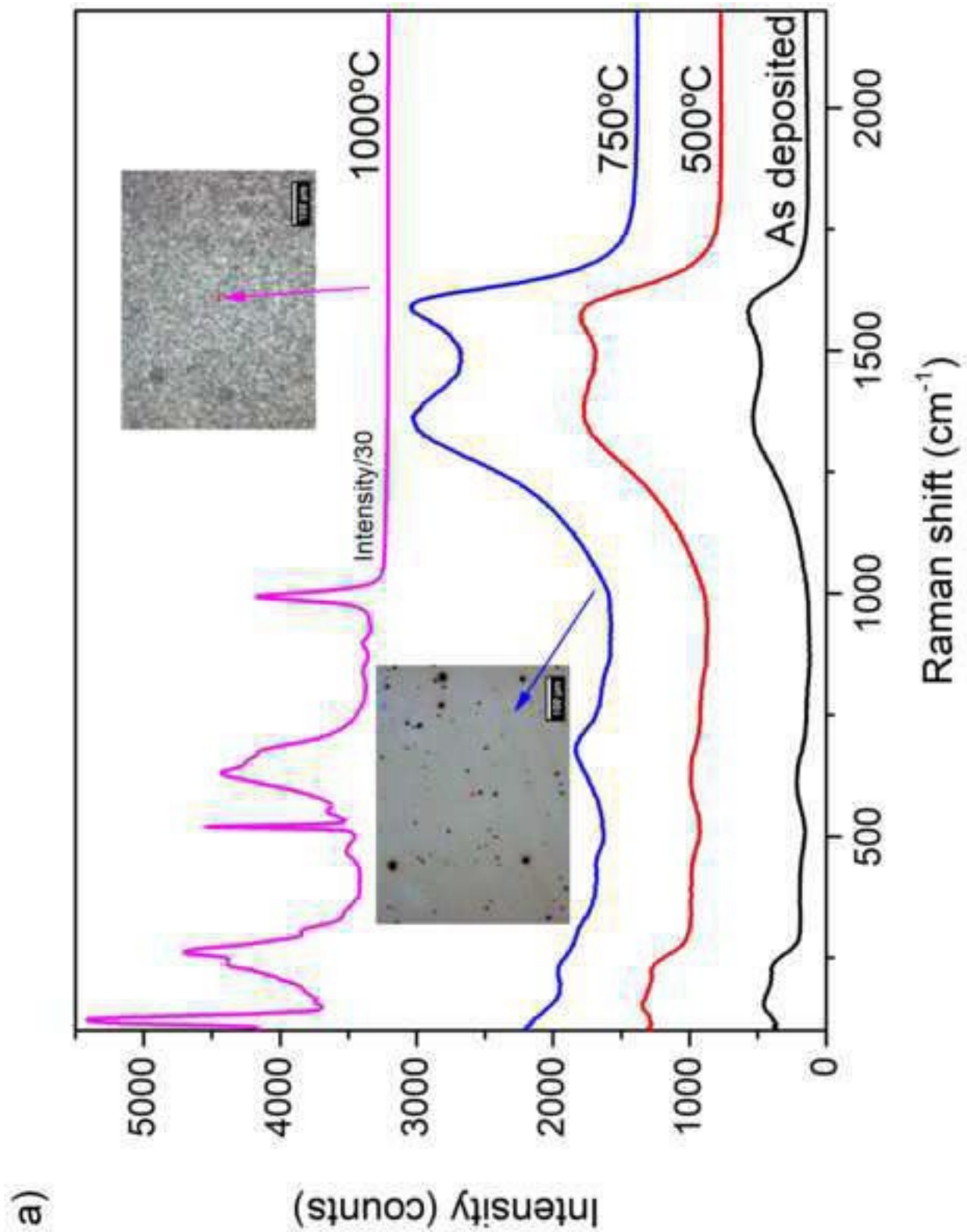

Figure 16a

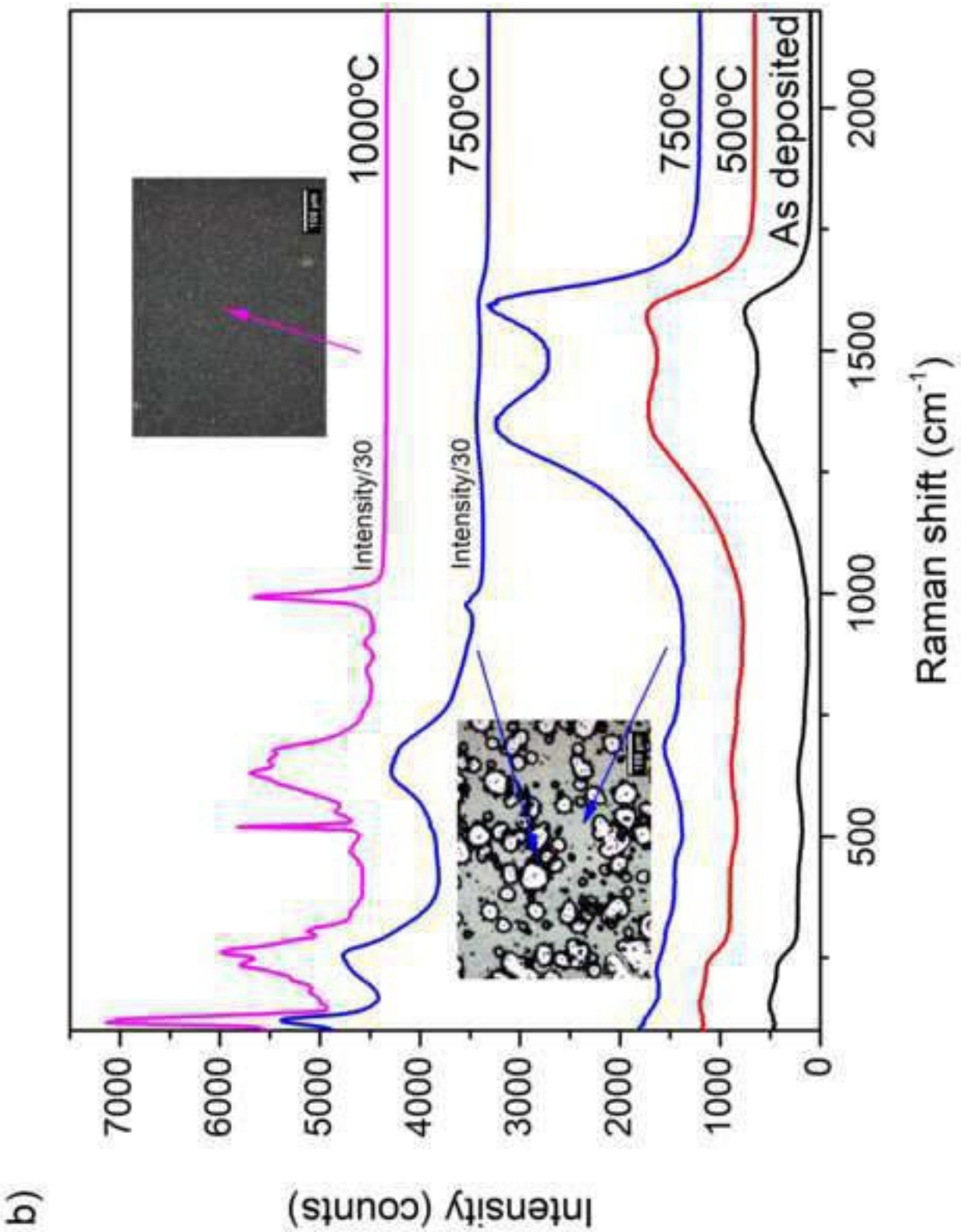

Figure 16b

This is a post-print (final draft post-refeering
Published in final edited form as
N. Sala, M. D. Abad, J. C. Sánchez-López, J. Caro, C. Colominas. Nb–C thin films prepared by DC-MS and HiPIMS: Synthesis, structure, and tribomechanical properties. En: *Surface and Coatings Technology.* 2021. Vol.422, p.127569.
Disponible a: https://doi.org/10.1016/j.surfcoat.2021.127569

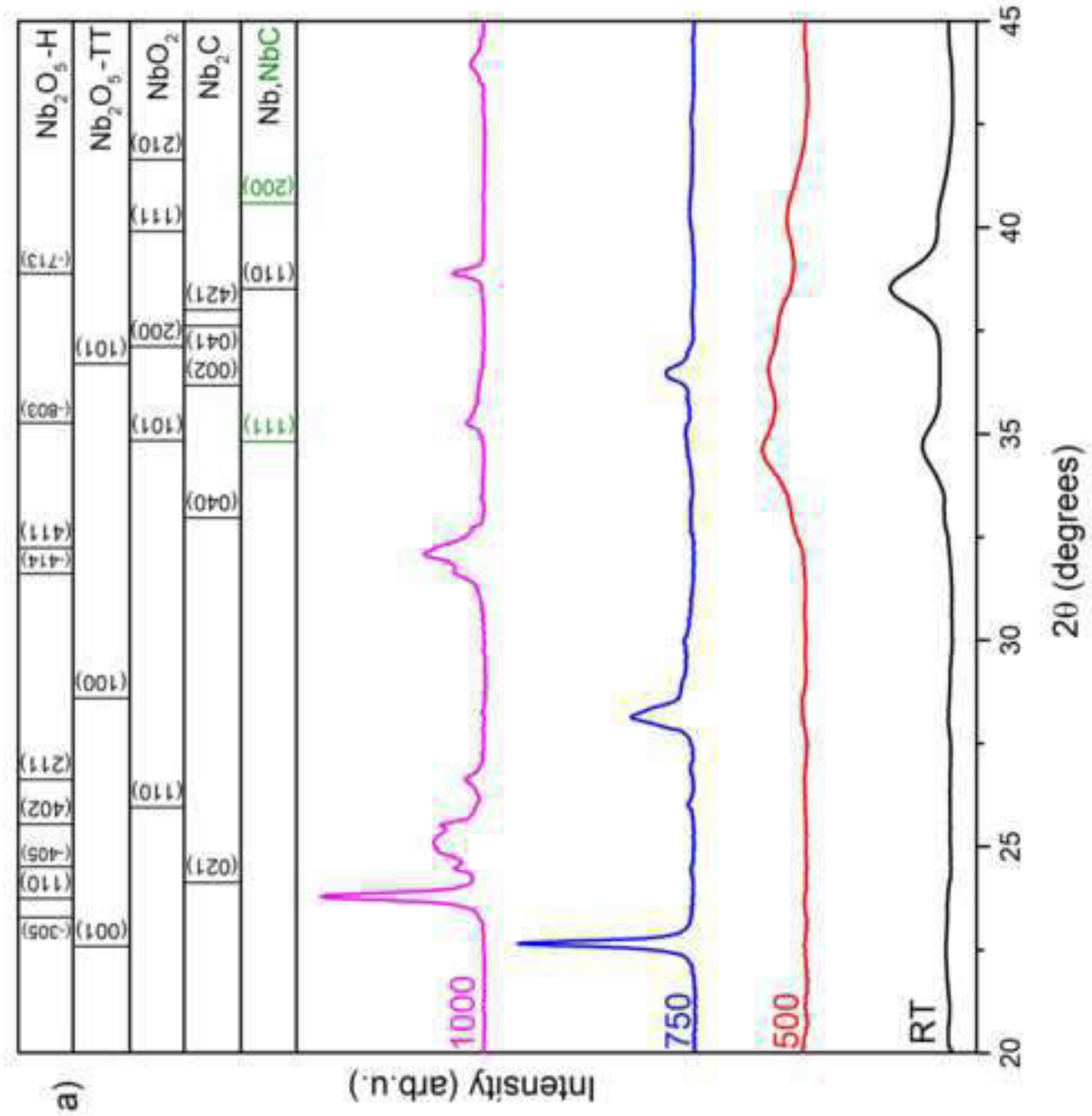

Figure 17a

This is a post-print (final draft post-refeering
Published in final edited form as
N. Sala, M. D. Abad, J. C. Sánchez-López, J. Caro, C. Colominas. Nb–C thin films prepared by DC-MS and HiPIMS: Synthesis, structure, and tribomechanical properties. En: *Surface and Coatings Technology.* 2021. Vol.422, p.127569.
Disponible a: https://doi.org/10.1016/j.surfcoat.2021.127569

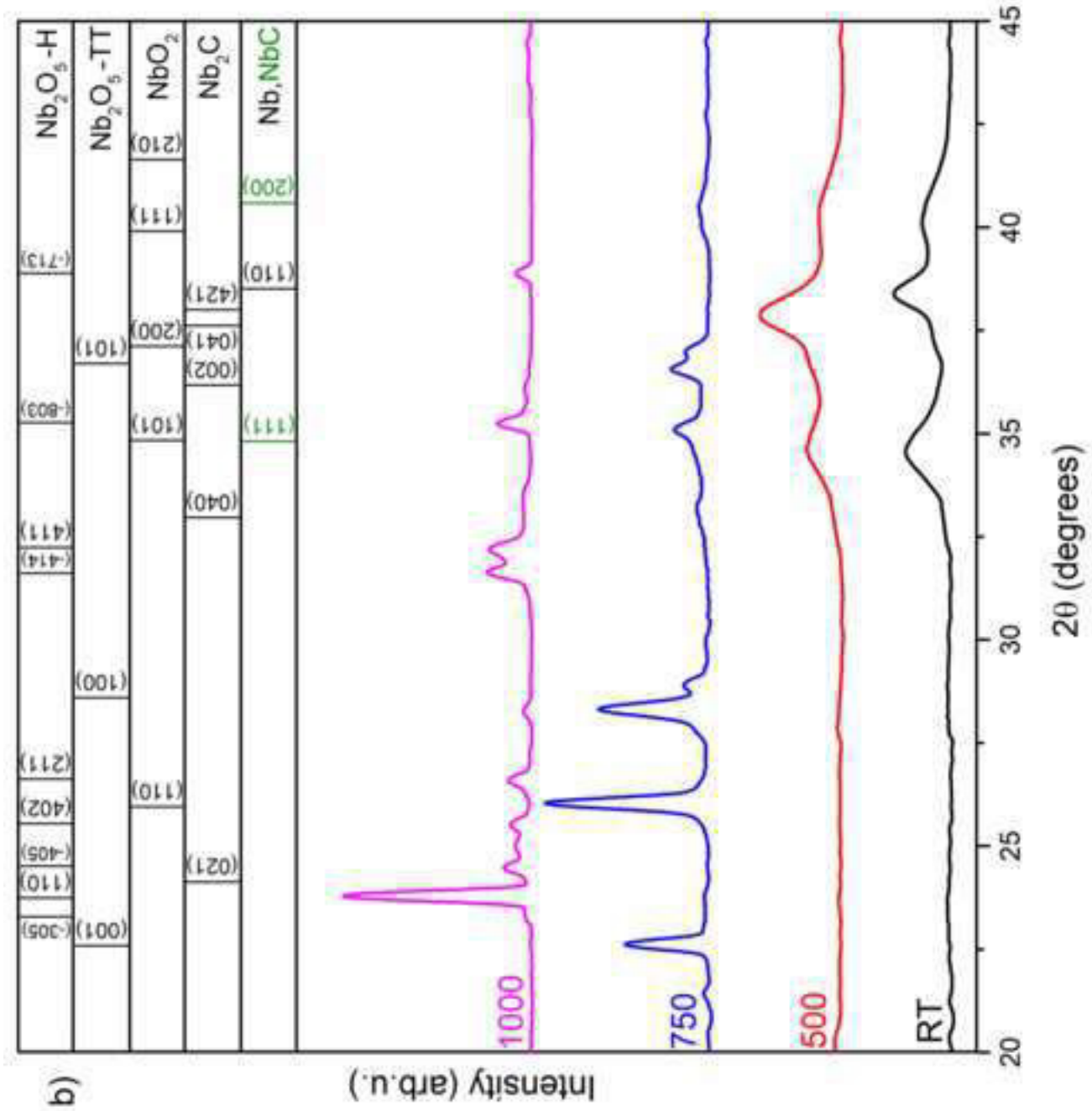

Figure 17b